Research Square

Preprints are preliminary reports that have not undergone peer review.
They should not be considered conclusive, used to inform clinical practice,
or referenced by the media as validated information.

# Comparative Assessment of Micro-Scale Heat Exchangers Operating in Flow Boiling

**Ali H. Al-Zaidi**
University of Misan
**Tassos G. Karayiannis**
tassos.karayiannis@brunel.ac.uk
Brunel University of London

**Research Article**

**Keywords:** Multi-channels, Micro pins, Micro-gap, Flow patterns, Two-phase flow, Heat transfer, Critical heat flux, Pressure drop

**Posted Date:** November 13th, 2026

**DOI:** https://doi.org/10.21203/rs.3.rs-11578799/v1

**License:** This work is licensed under a Creative Commons Attribution 4.0 International License.
Read Full License

**Additional Declarations:** No competing interests reported.

# COMPARATIVE ASSESSMENT OF MICRO-SCALE HEAT EXCHANGERS OPERATING IN FLOW BOILING

Ali H. Al-Zaidi[1] and Tassos G. Karayiannis[2*]

[1]*University of Misan, Al-Amarah, 62001, Iraq*
[2]*Centre for Energy Efficient and Sustainable Technologies,*
*Brunel University of London, Uxbridge,*
*UB8 3PH, UK*

[*]Address correspondence to Prof. Tassos G. Karayiannis, Department of Engineering, Brunel University of London, Uxbridge, Middlesex, UB8 3PH, UK.

Email: tassos.karayiannis@brunel.ac.uk

Phone Number: +44 (0) 1895 267132, Fax Number: +44 (0)1895 256392

## Abstract

The increasing demand to dissipate high heat fluxes from small areas in electronic equipment necessitated the move from air-cooled to liquid-cooled heat sinks and now to heat sinks operating in flow boiling. Researchers have intensified their efforts over the last few years and have examined and recommended various designs that fall into two main categories, namely rectangular, multi-micro-channel and micro pin fin heat exchangers. The research presented here describes experimental flow boiling work in these two geometries. A base benchmark design of a single micro-gap heat exchanger is also included. The base area of all three designs is the same to allow direct comparison of the heat dissipation capabilities for similar flow conditions. A dielectric HFE-7100 was used as the working fluid entering at 1 bar inlet pressure. The inlet subcooling was 5 K, the mass flux was varied between 100–300 kg/m$^2$ s and the wall heat flux up to 0.324 MW/m$^2$. In all experiments, the input heat was increased gradually until the exit vapour quality approached one or until near critical heat flux conditions were observed. A high-speed and high-resolution camera was used to visualise the flow boiling patterns. The comparison of the heat transfer results indicated that the micro pin fin heat sink provided better thermal performance than the other geometries. In both the micro-gap and the multi-channels, the dryout region, which precedes the critical heat flux, was reached at lower wall heat flux values than in the pin heat sink. In addition, flow reversal and system instability were found to be suppressed in this design. The pressure drop in the micro pin fin heat exchanger was higher, but it is worth noting that this is only a fraction of the total pressure drop and hence the pumping power of the thermal management system. Therefore, it does not constitute a restrictive parameter in design when, the designer needs to maximise the heat dissipation rate.

*Keywords: Multi-channels, Micro pins, Micro-gap, Flow patterns, Two-phase flow, Heat transfer, Critical heat flux, Pressure drop.*

## 1. Introduction

The thermal management market size for cooling high-heat flux devices has increased in the last decade due to the continuous growth of miniature electronic systems, artificial intelligence tools and internet of things, data centres, electric vehicles and charging stations and avionics systems in aircraft and space vehicles. The size of this global market was evaluated at USD 18.51 billion in 2026 and is expected to reach USD 43.42 billion by 2035 with an annual growth rate around 10% [1]. This means that this significant thermal challenge must be addressed to prevent overheating, component failure and maintain optimal performance. Fig. 1 depicts the thermal operating conditions of different applications that can generate moderate to extreme heat fluxes during operation. This figure was plotted here based on information reported in [2]–[9]. In addition it is worth noting that hot spots of computer chips and IGBTs can produce very high heat fluxes, around 50 MW/m$^2$, i.e. approaching the heat flux at the surface of the sun of approximately 63 MW/m$^2$ [10]. The above applications require efficient thermal management solutions, especially for the high-performance and micro-scale chipsets. Different thermal management solutions have been recommended, as depicted in Fig. 2. Some of these solutions are still under investigation and are not commercially available such as spray cooling and flow boiling (pumped two-phase) flow systems. The thermal management solutions covered in this figure were reported in detail in [11], [12], [21]–[27], [13]–[20]. The following summary can be deduced from this figure and the references provided:

1. Each thermal management solution can provide a different maximum thermal limit. For example, very low heat fluxes (smaller than 0.5 MW/m$^2$) can be achieved using free-convection heat sinks, forced-convection heat sinks, thermoelectric modules and heat pipes. This means that these cooling systems can no longer dissipate the moderate and high heat fluxes generated by modern equipment.
2. Different working fluids are used in these cooling systems such as air, water, R134a, R236fa, R410a, FC-72, HFE-7000 and HFE-7100. However, some of them are not recommended for electronics cooling due to thermal and/or environmental issues such as short-circuit fault (water), freezing expansion (damage in closed-loop systems due to high freezing point), high boiling point at atmospheric pressure, high global warming potential and high ozone depletion potential.
3. In certain experiments, extreme operating conditions were adopted to achieve high heat fluxes leading to more complicated and expensive cooling systems. For example, Sung and Mudawar [11] tested HFE-7100 in a hybrid system including multi-channels and micro-jets at very high inlet subcooling of 52–111 K. Their system provided a heat flux of 11.27 MW/m$^2$, which is the highest heat flux reported in the literature for this dielectric refrigerant at atmospheric working pressure. However, this value was reached at a fluid inlet temperature of -20 °C and inlet jet

velocity of 6.5 m/s. Thus, a second cooling system, i.e. low temperature refrigeration system, was used to maintain this high inlet subcooling condition.

4. The pumped two-phase thermal management solution can provide the highest thermal limits compared to the other geometries/arrangements in Fig. 2. In this system, different heat sink geometries, such as multi-channels or pins, and cooling techniques, such as flow boiling or spray cooling, can be used to increase the dissipated heat rates.

It can be concluded that pumped two-phase flow systems have a potential thermal performance capable of meeting current and future demands in dissipating the high thermal load that will prevail in high heat flux applications. These systems typically include a liquid reservoir, micro-pump, micro-evaporator block (the heat sink itself) and a micro-condenser as presented in Fig. 3. In addition, single or multiple micro-heat sinks can be utilised. Flow boiling taking place in the heat sink helps dissipate the required high thermal loads. The heat sink can be designed with different geometries and this is part of the study carried out here. This cooling solution has a number of advantages, namely: (i) High heat transfer coefficient and hence high heat dissipation rates compared to single-phase flows; (ii) During nucleate boiling, which is present with most refrigerants for a measurable length in the flow direction, the heat transfer coefficient increases as the required heat flux to be dissipated increases leading to an enhanced overall thermal performance; (iii) More uniform surface temperature distribution along the chipset compared to single-phase flows; (iv) Possible low degree of subcooling and low operating inlet pressure with appropriate selection of the refrigerant; (v) Small mass flow rates due to latent heat of evaporation; and (vi) Working fluids compatible with electronics. Acceptable design correlations of pressure drop and heat transfer coefficient are required in order to design this system. However, a significant discrepancy among the proposed correlations available in the literature is reported [2]. This is due to the fact that there are some fundamental issues that still need to be resolved. Different operating conditions such as inlet pressure, mass flow rate and inlet subcooling and the working fluid properties can affect the thermal performance of the micro-scale evaporators. In addition, heat sink geometry, i.e. channels of different aspect ratios, pins, gaps and more complicated shapes plus surface modifications (milling, laser texturing, 3D printing, nano-coating and artificial nucleation cavities), surface aging (contamination and thermal oxidation) can affect the flow boiling patterns, heat transfer rates and pressure drop results. For example, different sizes and shapes of pins and channels were examined in the literature leading to different heat transfer results, see [28]–[30]. Flow boiling instabilities and flow reversal, the appearance of dryout regions and critical heat flux depend on the above parameters and need to be considered. In an integrated thermal management system the size and the interaction of the micro-scale evaporators and the system condenser can also affect the results.

Different heat sink geometries have been studied in the literature using pins, parallel multi-channels and plain (gap) surfaces. To the best of the authors' knowledge, only the following studies have been found in the literature that compared these geometries. Chang et al. [31] examined sub-cooled flow boiling of FC-72 in three different heat sink geometries. They tested a plain surface as a reference

geometry and two in-line square pins heat sinks having a height of 0.07 mm and width of 0.1 mm and 0.2 mm. These geometries were manufactured on a silicon base area of 10 × 10 $mm^2$. The roughness measurement of these heat sinks was not mentioned. Flow boiling experiments were performed at a mass flux of 287–431 $kg/m^2$ s and inlet subcooling of 2.3–4.3 K. They found that, at a given wall superheat (wall-to-fluid temperature difference), pin fin heat sinks can achieve higher heat flux compared to the plain surface, i.e. the pin fin geometry gave higher single-phase and two-phase heat transfer coefficients. They attributed this thermal enhancement to the large heat transfer area by the pin fin heat sinks. Their results also confirmed that the pin fin geometry provided smaller bubble departure diameters, higher bubble departure frequencies and more active nucleation site densities than those observed on the plain surface. The above also contributed to the better thermal performance found in the pin fin geometry.

A saturated flow boiling study using R113 in two different heat sinks was performed by McNeil et al. [32]. Copper heat sinks with a base area of 50 × 50 $mm^2$ were manufactured in their study. They tested in-line square pins with 1 mm height and 1 mm width, and a smooth plain surface with 1 mm height. They did not report any details on surface roughness measurements of these two heat sinks. Their experiments were performed at a working pressure of 1 bar, mass flux from 50 to 250 $kg/m^2$ s and heat flux from 5 to 140 $kW/m^2$. They found that the pin fin geometry had slightly higher heat transfer coefficient than that in the plain surface and attributed this to the larger total heat transfer area in the pin geometry. Their flow visualisation results also showed that, at a heat flux of 80 $kW/m^2$, small bubbles flowing between pins were visualised, while dryout spots covering a large area in the plain surface were seen. Furthermore, they reported that the pin fin geometry had seven times higher pressure drop compared to the plain geometry.

Law and Lee [33] tested saturated flow boiling of FC-72 in parallel multi-channels and in-line oblique pin fin heat sinks made of copper. Forty rectangular channels with 1.19 mm height and 0.35 mm width were manufactured on a base area of 25 × 25 $mm^2$. Oblique pins with 1.17 mm height, 0.15 mm width and 27° angle were tested. Their experiments were conducted at a mass flux of 175–350 $kg/m^2$ s and an inlet fluid temperature of 29.5 °C. They did not report any roughness measurements in their study. Their results showed that the oblique pins provided higher heat transfer coefficient, lower instability, more uniform temperature distribution and higher critical heat flux compared to the multi-channels. This geometry also resulted in a higher pressure drop than that in the multi-channels. Law and Lee [33] attributed the thermal enhancement in the oblique pins heat sink to the high bubble generation introduced by these pins, and also due to the thin liquid film surrounding the pins as visualised by the high-speed camera.

Markal et al. [34] examined saturated flow boiling of deionized water in three different heat sink geometries, namely parallel multi-channels, in-line square pins and in-line square pins with a reduction number of pins in the flow direction (expanding flow passages). Micro pins having 0.5 mm width and 0.2 mm height were manufactured on a copper base area of 16 × 40 $mm^2$, while eleven parallel channels

with 0.5 mm width and 0.2 mm height were fabricated. The mass flux was 212 kg/m$^2$ s, the inlet fluid temperature was of 75 °C, which at an inlet pressure of 1 bar resulted in a 25 K degree of subcooling. No information on the surface roughness measurements of these heat sinks was mentioned in this study. They found that the pin fin geometry with expanding flow passages had a higher heat transfer coefficient by 365% and 501% compared to that in the simple pin geometry and the parallel channels, respectively. This was attributed to overcoming bubble confinement in the downstream region of the heat sink. Markal et al. [34] also found that this type of pin distribution supressed the system instability, and also reduced the two-phase pressure drop compared to the simple pin fin heat sink. Generally, the parallel multi-channels heat sink showed lower thermal performance, higher instability, but lower pressure drop compared to the two pin fin heat sinks.

Moreira et al. [35] carried out a flow boiling experimental study of deionized water in square pins and plain heat sinks. They manufactured two square pin fin heat sinks having 0.3 mm width and 0.35 mm height on a copper base area of 15 × 20 mm$^2$. These pins were fabricated to be in-line and staggered arrangements. A single channel (plain surface) with 0.75 mm depth was also tested as a reference heat sink. The average surface roughness of the plain surface was reported to be 0.17 μm, while no surface measurements were mentioned for the other heat sinks. They performed these experiments at a mass flux of 1000 and 1200 kg/m$^2$ s and inlet subcooling of 10 K and 20 K. Their study showed that the worst thermal performance was found in the plain heat sink. Moreover, at 1200 kg/m$^2$ s mass flux and 20 K subcooling, the in-line pin fin geometry had 64% higher heat transfer coefficient, while the staggered arrangement showed an increase of 35%, compared to the plain geometry. Moreira et al. [35] attributed this worst performance to the small total heat transfer area by the plain heat sink, and the fact that this heat sink provided fewer nucleation sites compared to other geometries examined.

Recently, Xie et al. [36] studied two-phase flow of HFE-7100 in three different heat sink geometries. They studied boiling flow patterns, heat transfer coefficient and pressure drop using parallel multi-channels, staggered square pins and in-line square pins. A copper block was used to manufacture these heat sinks at a base area of 9.5 × 15 mm$^2$. The fin height and width were designed to be 0.5 mm. They conducted their experiments at atmospheric pressure, heat flux of 10–396 kW/m$^2$, mass flux of 89–278 kg/m$^2$ s and inlet subcooling of 20.8–35.8 K. They reported that the flow patterns found in their study were bubbly, slug, churn, annular and dryout. However, slug flow was only visualised in the multi-channels heat sink, while churn flow occurred in both pins heat sinks. Their results also showed that the pins heat sinks had higher thermal performance compared to the multi-channels, with the in-line arrangement providing the best results. The pressure drop results showed that, at low heat fluxes when bubbly flow dominated in all these heat sinks, there was no a clear difference in these geometries. However, at high heat fluxes when slug flow occurred in the multi-channels and churn flow established in the pin fin heat sinks, both the pin fin heat sinks had higher pressure drop compared to the multi-channels heat sink. At highest heat fluxes, the geometry effect was also found to be insignificant on the pressure drop due to the same flow regime (dryout) occurred in all these heat sinks.

Yu et al. [37] carried out a flow boiling study of deionized water in parallel multi-channels, staggered square pins and in-line square pins. These heat sinks were made of copper at a base area of 25 × 25 $mm^2$. The height and width of these fins were manufactured at 1 mm and 0.5 mm, respectively. Their experimental study was performed at a heat flux of 100–2400 $kW/m^2$, mass flow rate of 0.002, 0.004 and 0.006 kg/s and inlet subcooling of 30 K and 70 K. They found that, by comparing the pin fin results to the multi-channels, the average heat transfer coefficient increased up to 15.6% and 22.5% for the in-line and staggered pins, respectively. They mentioned that pins can enhance the wall rewetting process and delay dryout on the walls. They also reported that this geometry supressed the vapour backflow towards the heat sink inlet. The two-phase pressured drop was found to decrease by 42.1% for the staggered pins and 45.5% for the in-line arrangement compared to the straight channels. They attributed this result to the fact that the pins arrangement could provide larger flow passages compared to the straight channels.

Although the above-mentioned studies showed that pin fin heat sinks can provide better thermal performance than other geometries, the total surface area or/and the surface roughness measurements were not kept constant or were not mentioned at all. It is well-known that these two parameters could significantly affect the flow boiling phenomenon in micro-scale heat sinks. In view of the above, the contribution of the present study is outlined as follows:

1. The investigation of the effect of different heat sink geometries (micro-gap, multi-channels and micro pins) on the two-phase flow patterns, pressure drop and heat transfer coefficient. These three heat sinks have the same base area of 20 × 25 $mm^2$ and channel height of 1 mm. Both the multi-channels and the micro pin fin heat sinks were carefully designed at the same fin width of 0.6 mm, hydraulic diameter nearly 1 mm and total heat transfer area of 0.001 $m^2$. Therefore, the effect of the design geometry can be studied for the same heat transfer area.
2. All three heat sinks were manufactured using a high precision milling machine at nearly the same machining settings. This ensured the same surface finish for all heat sinks, i.e. approximately the same roughness parameters, hence this was not affecting the comparative results.
3. HFE-7100 as a good coolant for most electronics with acceptable environmental properties was selected. All the flow boiling experiments were conducted at 1 bar, very low degree of subcooling of 5 K, low range of mass fluxes of 100–300 $kg/m^2$ s and heat flux up to the maximum thermal limits, i.e. at exit vapour quality of one or Critical Heat Flux (CHF). These low operating conditions were chosen to reduce the energy consumption, condenser size and system complexity of a possible thermal management system.
4. Flow visualisation along the entire heat sink was performed using a high-speed camera. The effect of different control parameters on the two-phase flow patterns were analysed and discussed.

5. The present study also includes a comparison between flow boiling and single-phase systems for electronics cooling.

## 2. Experimental facility and data reduction

Fig. 4 shows the experimental facility used in this study including water-glycol cooling loop and the working fluid loop. HFE-7100 was examined at different operating conditions by conducting single-phase and two-phase flow experiments. More details about this facility can be found in [38]. Flow visualisation was carried out using a Phantom, high-resolution, high-speed camera (Miro-C210) with a microscope mounted with a LED lighting system. A micro-milling machine model HERMLE C20U was used to manufacture the test sections. This included six parts made from different materials: oxygen-free copper, PTFE and Polycarbonate as shown in Fig. 5(a). The heat sink block was made of the oxygen-free copper with a total height of 40 mm as shown in Fig. 5(b). Three horizontal heat sinks having different geometries were designed and fabricated, see Fig. 5(c). A micro-gap heat sink as a flat (plain) surface with 1 mm height was designed in the present study. This design was chosen here since it is a simple heat sink that is used as a benchmark compared to other geometries. This wide surface area without flow disruption can also provide better flow visualisation, allowing the flow features to be easily visualised and understood. Rectangular multi-channels were also adopted, being the most-commonly design reported in literature. Finally, a staggered diamond micro pin fin heat sink was designed and fabricated. Details on the dimensions and surface roughness of the three heat sinks are given in Table 1. They all have the same base area of 20 × 25 mm$^2$ and channel height of 1 mm. Other design criteria were also considered here to isolate the effect of channel hydraulic diameter and total heat transfer area. For example, the hydraulic diameter of the multi-channels and the micro pins was designed to be nearly 1 mm resulting in both cases to a total heat transfer area of 0.001 m$^2$. This is an essential design step to eliminate the effect of the heat transfer area when comparing these two heat sinks. The surface roughness measurements of these heat sinks were conducted using the 3D Surface Metrology System. *Ra* and *Sa*, measurements, taken at different locations along the bottom surface and then averaged, were found to be 0.102–0.151 μm and 0.103–0.132 μm, respectively. Therefore, the three heat sinks have nearly the same surface roughness parameters due to the fact that the same material, milling process and machining settings were used.

For the multi-channels, the Fanning friction factor in single-phase flow experiments is calculated using Eq. (1–3).

$$f = \frac{\Delta P_{ch} \rho_l D_h}{2 G_{ch}^2 L_{ch}} \tag{1}$$

$$\Delta P_{ch} = \Delta P_{meas} - (\Delta P_{sc} + \Delta P_{se}) \tag{2}$$

$$G_{ch} = \frac{\dot{m}}{N_{ch} H_{ch} W_{ch}} \tag{3}$$

The measured pressure drop $\Delta P_{meas}$ is obtained from the differential pressure transducer, while the pressure loss components due to sudden contraction and expansion $\Delta P_{sc}$ and $\Delta P_{se}$ are described in detail in [39], [40]. The local single-phase heat transfer coefficient and then the average value are calculated using Eq. (4–5), while the Nusselt number is found from Eq. (6).

$$h_{sp(z)} = \frac{q"_w}{T_{w(z)} - T_{l(z)}} \tag{4}$$

$$\overline{h_{sp}} = \frac{1}{L_{ch}} \int_0^{L_{ch}} h_{sp(z)} \tag{5}$$

$$\overline{Nu} = \frac{\overline{h_{sp}} D_h}{k_l} \tag{6}$$

It is worth-mentioning that five horizontal K-type thermocouples were inserted (at 10 mm depth) underneath the heating surface and along the heat sink. These five locations are used to conduct the present local calculations. The wall temperature $T_{w(z)}$ and the liquid temperature $T_{l(z)}$ at specific location are found as follows:

$$T_{w(z)} = T_{th(z)} - \frac{q"_b}{k_{cu}} y \tag{7}$$

$$T_{l(z)} = T_{in} + \frac{q"_w (2H_{ch} + W_{ch}) z N_{ch}}{\dot{m} c p_l} \tag{8}$$

$T_{th(z)}$, $T_{in}$, $y$ and $z$ are the local temperature given by thermocouples underneath the channel surface, the inlet liquid temperature (measured by T-type thermocouple at the channel inlet), the vertical distance between the channel surface and the first raw of thermocouple centre, and the local distance measured from the channel inlet, respectively. The base heat flux and then the wall heat flux are calculated from Eq. (9–12).

$$q"_b = k_{cu} \frac{dT}{dy} \tag{9}$$

$$q"_w = \frac{q"_b A_b}{(2\eta_f H_{ch} + W_{ch}) L_{ch} N_{ch}} \tag{10}$$

$$\eta_f = \frac{\tanh(mH_{ch})}{mH_{ch}} \tag{11}$$

$$m = \sqrt{\frac{2h_{(z)}}{k_{cu} W_f}} \tag{12}$$

The temperature gradient $\frac{dT}{dy}$ ,obtained using thermocouple values at five vertical locations, is used to find the base heat flux during the experiments by assuming 1D heat conduction. The base area $A_b$ in the present heat sinks is 20 × 25 mm$^2$. In above two-phase flow experiments, the local two-phase heat transfer coefficient is calculated from Eq. (13), and then the average two-phase heat transfer coefficient is calculated from Eq. (14).

$$h_{tp(z)} = \frac{q"_w}{T_{w(z)} - T_{sat(z)}} \tag{13}$$

$$\overline{h_{tp}} = \frac{1}{L_{ch} - L_{sub}} \int_{L_{sub}}^{L_{ch}} h_{tp(z)} \tag{14}$$

The saturation temperature $T_{sat(z)}$ at a specific location is found at the local saturation pressure using the saturation fluid-curves in the EES software. The pressure drop is assumed to be linear along the heat sink to help find this local saturation pressure. The subcooled length $L_{sub}$ is found from Eq. (15) at the saturation temperature of the subcooled length $T_{sat(sub)}$ corresponding to the saturation pressure of the sub-cooled region $P_{sat(sub)}$ from Eq. (16).

$$L_{sub} = \frac{\dot{m} c_{p_l} (T_{sat(sub)} - T_{in})}{q"_w (2H_{ch} + W_{ch}) N_{ch}} \tag{15}$$

$$P_{sat(sub)} = P_{in} - \frac{2 f_{sp} G^2 L_{sub}}{\rho_l D_h} \tag{16}$$

In the above, $P_{in}$ is the inlet pressure measured by a pressure transducer placed at the channel inlet. The Fanning friction factor $f_{sp}$ is found based on the channel geometry and flow regime, see [39], [40]. Eq. (17) is then used to calculate the two-phase pressure drop.

$$\Delta P_{tp} = \Delta P_{ch} - \Delta P_{sp} \tag{17}$$

The vapour quality $x_{(z)}$ is calculated locally using Eq. (18). This equation is also used to find the exit vapour quality at the outlet conditions.

$$x_{(z)} = \frac{i_{(z)} - i_{l(z)}}{i_{lg(z)}} \tag{18}$$

The local specific enthalpy is given by:

$$i_{(z)} = i_{in} + \frac{q"_w (2H_{ch} + W_{ch}) z N_{ch}}{\dot{m}} \tag{19}$$

The abovementioned calculations are also used for the micro-gap heat sink at the channels number $N_{ch}$ set to one, see [41]. Similar procedure is also adopted in the micro pin fin geometry, as explained in detail by [40]. The uncertainties in the measured and calculated variables are calculated according to [42], see Eq. (20) and Table 2.

$$U_r = \sqrt{\left\{\frac{\partial r}{\partial X_1} U_{X1}\right\}^2 + \left\{\frac{\partial r}{\partial X_2} U_{X2}\right\}^2 + \cdots + \left\{\frac{\partial r}{\partial X_j} U_{Xj}\right\}^2} \tag{20}$$

In Eq. 920 above $X_1$ and $X_j$ are the measured parameters having uncertainties of $U_{X1}$ and $U_{Xj}$. Error bars are also included in all the present figures. The standard deviation of the measured pressure drop signal is calculated to assess flow instability (flow oscillations) as follows:

$$\sigma(\Delta P) = \sqrt{\frac{\sum_{n-1}^{n} (P_n - \bar{P}_n)^2}{n}} \tag{21}$$

$n$ denotes the number of data points. The energy consumed by the pump is calculated from Eq. (22).

$$Q_p = \frac{\dot{m}\Delta P_{ch}}{\rho_l \eta_p} \tag{22}$$

The pump efficiency $\eta_p$ is assumed to be 80% in the present analysis. The cooling capacity is also calculated as follows:

$$Q_{cc} = q"_b W_b L_b \tag{23}$$

where $W_b$ and $L_b$ are the base width of the heat sink (20 mm) and the base length (channel length of 25 mm), respectively. A degassing process was conducted to ensure that there was no air trapped in the experimental facility. Single-phase flow experiments were then carried out to commission and validate all the sensors of the experimental rig. The two-phase flow experiments were performed at an inlet pressure of 1 bar, inlet subcooling of 5 K, mass flux of 100–300 kg/m$^2$ s and wall heat flux up to around 324 kW/m$^2$. This heat flux was gradually increased until the exit vapour quality of one, or the critical heat flux was reached.

## 3. Results and discussion

### *3.1 Single-phase validation*

Single-phase flow validation was performed for all three heat sinks. Here we present the results for the multi-channels heat sink. Fig. 6 shows the present single-phase using diabatic and adiabatic experiments. The correlations of Shah and London [43] and Copeland [44] provided a very good prediction of the present friction factor results with a mean absolute error of 9% and 15%, respectively, see Fig. 6(a). The present Nusselt number results also showed good agreement with the correlations of Jiang et al. [45] and Lee and Garimella [46] with a MAE of 9–23%, as shown in Fig. 6(b). Similar comparison resulted for the micro-gap and the micro pin fin heat sinks, i.e. single-phase results were in a good agreement with past correlations both in terms of the friction factor and the Nusselt number predictions, see [40], [41]. Therefore, it was concluded that the experimental facility used is well validated for the present flow boiling studies.

### *3.2 Flow boiling patterns*

The Phantom high-speed camera was adopted to visualise the flow patterns along the heat sinks and at different operating conditions. The camera was set at 512 × 512 pixel and 3500 fps for the multi-channels and the micro pin fin heat sinks, while these settings were changed to 1280 × 1024 pixel and 1800 fps for the micro-gap heat sink to capture a wider area. The visualisation locations along the heated length are presented in Fig. 7.

#### *3.2.1 Flow patterns in the micro-gap heat sink*

The supplied heat flux was set at very low values to clearly visualise the features of flow patterns at the onset of boiling. Fig. 8 depicts different wall heat fluxes at an inlet pressure of 1 bar and mass flux

of 100 kg/m$^2$ s. At low heat flux of 39 kW/m$^2$, most of the bottom surface was not active, while some nucleating bubbles originated at the edge of this heat sink, see Fig 8(a) indicating that these sharp edges can promote nucleation. When the heat flux increased to 58.6 kW/m$^2$, a larger number of bubbles originated from the bottom surface as shown in Fig. 8(b). It is interesting to know that these nucleating bubbles formed at the surface feed marks. A close-up image of the surface depicted in Fig. 8(c) verified that these feed marks had grooves and peaks. These grooves could behave like tiny channels, promoting more nucleation sites.

The present flow visualisation results at 1 bar inlet pressure, 100 kg/m$^2$ s mass flux and different heat fluxes is shown in Fig. 9. Three main flow patterns were observed, namely bubbly, mixed and vapour layer flow. At 83 kW/m$^2$, bubbly flow is seen in this figure as a number of small and round bubbles formed on the surface and travelled in the liquid flow. Mixed flow was seen at 137 kW/m$^2$ as larger bubbles mixing with liquid phase flow. A dryout spot underneath these large bubbles was captured during this flow regime. Vapour layer flow was visualised when the heat flux was 167 kW/m$^2$. This flow regime occurred due to the collision of large vapour bubbles. At these operating conditions, liquid straps and dryout areas on the bottom surface can clearly be seen. These liquid straps formed on the heated surface as a thin liquid film surrounded by large dryout spots, see the red dashed lines. These liquid straps were found to shrink with time due to the evaporation process leading to an increase in the dryout areas on the surface.

Fig. 10 shows other interesting features during bubbly flow visualised in this geometry when the heat flux was set at 72 kW/m$^2$. It can be seen that, at a designated time of 0 ms, nucleating bubbles occurred on this surface, which flow towards the outlet, as indicated by the yellow arrow. After 10 ms, a vapour layer formed at the edge and tended to move towards the centre of the heat sink. In addition, some dryout spots can be captured in this layer at 20 ms. At 65 ms, a second vapour layer with a dryout spot occurred at the opposite edge. High generation of nucleating bubbles and coalescence rates at these edges can lead to the appearance of large vapour layers. The rapid bubble generation at the edges led to the entire flow being pushed in a zig-zag motion, see the yellow arrows in this figure. It is interesting to know that, flow reversal was not seen in the micro-gap heat sink.

### *3.2.2 Flow Patterns in the multi-channels heat sink*

Different features of flow patterns were visualised at a system pressure of 1 bar and mass flux of 300 kg/m$^2$ s as shown in Fig. 11. Bubbly flow was observed at this location with bubbles origination from the bottom surface and the wall-edges when the wall heat flux was set at 88.5 kW/m$^2$. This large number of bubbles had a smaller size than the channel width and were firstly seen to form at the wall-edges of the multi-channels. The angle between the side-wall of the channel and the bottom surface could trap the vapour and act as an active nucleation site. Slug flow occurred when the heat flux increased to 120 kW/m$^2$. The vapour slugs having rounded tips were similar in size to the channel width. Some long vapour slugs followed by small bubbles were visualised at this location. Confined bubbles could expand

in both directions, i.e. towards the channel inlet and outlet; a phenomenon that can lead to flow reversal within these micro-channels, see also [38]. Some small nucleating bubbles were also found in the liquid film between the surface and the vapour interface. Churn flow, as a mixture of vapour and liquid, occurred at a heat flux of 197 kW/m$^2$. When the heat flux increased to 300 kW/m$^2$, annular flow was found as a vapour core surrounded by a liquid film. A very thin liquid film, seen as a dark layer, between the channel sidewalls and the vapour core was visualised by the present camera, see Fig. 11.

### *3.2.3 Flow patterns in the micro pins heat sink*

The flow patterns along this heat sink were presented in Fig. 12. At the heat sink inlet, nucleating bubbles were found to form at the wall-edges of the pins, indicating that an increased pin density will favour bubble generation. These bubbles were seen to move forward, passing between the pins. Mixed flow with large bubbles and liquid was visualised at the middle of the heat sink. Active nucleation sites around the pins can also be seen in this flow regime. At the heat sink outlet, a vapour layer flow developed both on the surface and between the pin arrays. Some nucleating bubbles in the liquid film around these pins can still be found. A zig-zag flow without flow reversal was also seen in this geometry; further analysis is provided by [40].

The above-mentioned discussion showed that distinct, different flow regimes occurred in each heat sink. Bubble generation at the inlet, followed by bubble coalescence at the middle and outlet, and a reduction in the local pressure along the heated length can lead to these subsequent flow patterns. Summarising, it can be concluded that; (i) both the multi-channels and the micro pin fin heat sinks provided more nucleation sites than those observed in the micro-gap heat sink. An increased number of channels or pins can promote a higher number of nucleating bubbles, (ii) dryout spots clearly formed on the surface and along the micro-gap heat sink, (iii) zig-zag flow was visualised in the micro-gap and the micro pin fin heat sinks, (iv) flow reversal occurred in the multi-channels, and (v) the micro pin fin heat exchanger offered the larger number of nucleation sites, even at the outlet location and at high heat fluxes.

## *3.3 Two-phase heat transfer results*

This section discusses the experimental heat transfer results by presenting and discussing the boiling curve, the local heat transfer coefficient along the heated length and the average two-phase heat transfer coefficient at different operating conditions for each geometry.

### *3.3.1 Heat transfer in the micro-gap heat sink*

Fig. 13(a) shows the boiling curve of HFE-7100 in the micro-gap heat sink at three different mass fluxes. As seen in the figure, the onset of nucleate boiling (ONB) occured at low wall heat flux, around 30 kW/m$^2$. Subsequently, the wall heat flux increased with temperature difference ($T_w - T_{sat}$) with a

sudden jump in the temperature difference when the dryout region is reached. The CHF can clearly be identified in this figure. The mass flux had an insignificant effect on the wall heat flux within the range studied. However, it should be noted that increasing mass flux led to an increase the possible range of CHF. A maximum wall heat flux of 232 kW/m$^2$ was reached when the mass flux was set at 200 kg/m$^2$ s. The local heat transfer coefficient versus the local vapour quality is also presented in Fig. 13(b-c). The corresponding local flow patterns related to these is also presented in the figure. It can be seen that maximum local two-phase heat transfer coefficient occurred at very low local vapour qualities, in the presence of bubbly flow. The local two-phase heat transfer coefficient reduced along the heated channel, when this flow pattern changed to mixed flow or vapour layer flow. It is also seen in the figure that increasing wall heat flux led to an increase in the local two-phase heat transfer coefficient, while the mass flux resulted in an insignificant effect. The average two-phase heat transfer coefficient versus the wall heat flux is presented in Fig. 13(d). It is clearly seen that increasing wall heat flux resulted in an increase in the average heat transfer coefficient until the dryout region occurred, when a clear reduction was found. The mass flux had no effect on the average two-phase heat transfer coefficient but as mentioned above, it can extend the CHF to higher values.

### *3.3.2 Heat transfer in the multi-channels heat sink*

The experimental boiling curve of the multi-channels heat sink is shown in Fig. 14(a). This figure covers a wall heat flux of 8–308 kW/m$^2$ and temperature difference up to 36 K. As seen in the figure, the ONB started at a low temperature difference, i.e. around 5 K. After that, the wall heat flux increased monotonically with increasing temperature difference. Fig. 14(a) illustrates that, for a given temperature difference, increasing mass flux from 100 to 300 kg/m$^2$ s did not affect the wall heat flux. However, as above for the micro-gap, the possible CHF was found to increase with increasing mass flux. For example, the maximum wall heat flux, verified by the rapid change in temperature difference, was 136, 265 and 308 kW/m$^2$ at a mass flux of 100, 200 and 300 kg/m$^2$ s, respectively. Law and Lee [33] and Kosar and Peles [47] reported that the CHF was found to increase with increasing mass flux, which is similar to our findings. The local heat transfer coefficient variation with local vapour quality and different wall heat flux and mass flux is presented in Fig. 14(b-c). A higher local two-phase heat transfer coefficient can be seen at very low local vapour quality for a given heat or mass flux. This was found to decrease with increasing local vapour quality along the heat sink. The transition in flow patterns along the heated length as presented in this figure, i.e. from bubbly flow (high nucleation at the inlet) to slug, churn and then annular flow (with reduction or suppression of nucleation) could lead to this local reduction in the heat transfer coefficient [38]. This figure also illustrates that increasing wall heat flux from 78 to 242 kW/m$^2$ led to an increase in the local two-phase heat transfer coefficient by activating more nucleation sites on the surface. The maximum local two-phase heat transfer coefficient was found to be 13.29 kW/m$^2$ K at these operating conditions. The mass flux effect on the local heat transfer coefficient was insignificant in the range studied, i.e. 100–300 kg/m$^2$ s. The average two-phase

heat transfer coefficient of the multi-channels heat sink is depicted in Fig. 14(d). It can be seen that, for a given mass flux, an increase in the wall heat flux led to an increase in the average two-phase heat transfer coefficient. However, a noticeable reduction in the average two-phase heat transfer coefficient can be seen during the dryout region. Flow visualisation results demonstrated that increasing wall heat flux promoted more nucleation sites on the surface until the dryout areas in the annular flow occurred leading to this reduction. This figure also shows that increasing mass flux from 100 to 300 kg/m$^2$ s had an insignificant effect. However, the CHF increased with mass flux, indicating the importance of this design in the upper limit of operation of the heat sink. The maximum average two-phase heat transfer coefficient was 13.43 kW/m$^2$ K at wall heat flux of 275 kW/m$^2$ and mass flux of 300 kg/m$^2$ s.

### *3.3.3 Heat transfer in the micro pins heat sink*

The experimental heat transfer results using the micro pins are presented in Fig. 15. Further details and discussion can be found in [40]. These are similarities with the findings for the micro-gap and the micro-channels heat sink. The wall heat flux increased monotonically with temperature difference, without a mass flux effect, see Fig. 15(a). In addition, the local and the average heat transfer coefficient increased with the applied heat flux. High local heat transfer coefficient measurements were found at the inlet of this heat sink, i.e. at low local vapour qualities where bubbly flow is the dominant flow regime as shown in Fig. 15(b-c). The mass flux had no effect on the heat transfer results, see Fig. 15(d), while it showed a clear effect on the possible maximum heat flux, again pointing out to the possible importance of this parameter in deciding the operational limits of the heat sink. One of the noticeable differences between these results and the results found in the other geometries is the fact that the dryout region and then the critical heat flux conditions were not reached in this geometry for the range studied, i.e. this geometry can deliver higher thermal operational limits. Maximum wall heat flux was reached at 324 kW/m$^2$ at a maximum mass flux of 250 kg/m$^2$ s as shown in these results.

### *3.3.4 Heat transfer rates comparison in the three geometries*

Fig. 16(a) shows the boiling curve of three heat sinks at a system pressure of 1 bar and mass flux of 100 kg/m$^2$ s. For a given temperature difference, the micro pin fin heat sink provided higher wall heat fluxes than the other heat sinks, with the lowest values reached in the micro-gap. At these operating conditions, the maximum wall heat flux was recorded at 136, 167 and 180 kW/m$^2$ for the multi-channels, the micro-gap and the micro pin fin heat sink, respectively. However, as seen in the figure, the micro pin fin heat sink can reach heat fluxes beyond 180 kW/m$^2$, without reaching CHF conditions. These results can clearly be linked to the different features of flow patterns discussed in Section 3.2. The pin fin geometry can promote higher nucleation rates around their perimeter, even at high heat fluxes, i.e. nucleation in the liquid film surrounding these pins. They also result in better mixing of the liquid and vapour generated. This could prevent dryout spots forming on the surface and enhance the

thermal performance. In contrast, dryout spots were observed on the micro-gap surface even at the inlet, while also seen in the liquid film of the annular flow in the multi-channels.

Fig. 16(b) shows the local heat transfer coefficient versus the dimensionless axial location for the three geometries at a wall heat flux around 100 kW/m$^2$ and mass flux of 100 kg/m$^2$ s. The pin fin geometry provided the highest local two-phase heat transfer coefficients with the micro-gap heat sink demonstrating the lowest values. As discussed in Section 3.2, at the inlet, a large number of small bubbles can be seen in the micro pin fin heat sink, with a smaller number of larger bubbles captured in the multi-channels. Nucleating bubbles but with some dryout spots on the surface were recorded at the inlet of the micro-gap. At the outlet, a liquid film with numerous nucleation sites around the pin perimeter without dryout was seen, enhancing the evaporation and heat transfer process. In contrast, a liquid film with a small number or completely supressed nucleation sites were seen during the annular flow in the multi-channels, and clearly seen dryout areas on the micro-gap surface had a significant diminishing effect on the local surface temperatures and the local two-phase heat transfer coefficients.

Fig. 16(c) illustrates that all the three heat sinks showed an increase in the average two-phase heat transfer coefficient with heat flux, as discussed before. However, in the micro-gap and the multi-channels heat sinks, the heat transfer coefficient decreased in the dryout region leading to CHF. At a given wall heat flux, the micro pin fin heat sink showed higher average two-phase heat transfer coefficient compared to the micro-gap and the multi-channels heat sinks without reaching CHF in the ranged studied.

Uniform surface temperature distribution along the entire heat sink is another design criterion to consider in electronics. Non-uniform and high surface working temperature along the heat sink, and hence the electronic substrate to be cooled, could lead to high thermal stress and then thermal failure. Accordingly, this temperature distribution for the different design geometries was examined in Fig. 16(d). The local wall temperature at five locations along the heated length was plotted at an inlet pressure of 1 bar, wall heat flux around 115 kW/m$^2$ and mass flux of 100 kg/m$^2$ s. In this figure, $\Delta T_w$ represents the difference between the lowest temperature (1$^{st}$ location) and the highest temperature (5$^{th}$ location). The average wall temperature $\bar{T}_w$ was calculated by taking into account all these five locations. As depicted in this figure, the local wall temperature increased along the heated length for all heat sinks. The nucleation process diminishes along the heat sink with the occurrence of the subsequent flow regimes, see Section 3.2, which could lead to an increase in the local surface temperature along the heat sink. However, the variation in wall temperature is different in the three heat sinks. The temperature difference across the micro pin fin, micro-gap and multi-channels heat sinks was found to be 0.7 K, 0.8 K and 1.5 K, respectively. Furthermore, at these operating conditions, the average wall temperature of the micro pin fin, multi-channels and micro-gap heat sinks was measured at 73 °C, 76 °C and 82 °C, respectively. This low average surface temperature and temperature difference along the micro pin fin heat sink is due to the higher number of nucleation sites and good fluid mixing, which can reduce the number of dryout spots, as discussed above. In contrast, a small number of nucleation sites

with clear dryout spots along the micro-gap heat sink, even near the inlet, could lead to this high average surface temperature. In the multi-channels, bubbly flow was clearly visualised at the inlet, then slug, churn and annular flow occurred towards the outlet. The high number of nucleation sites near the inlet, with the number reducing along the flow direction, with possible dryout spots during annular flow at the outlet can result in a noticeable temperature difference. This can also be seen at the last three local thermocouples, i.e. these locations had higher temperatures than the first two locations.

From the perspective of the design of cooling of electronics, the base heat flux should be identified here, as it directly represents the thermal power dissipated by chipsets. Therefore, the experimental boiling curve was re-plotted using the base heat flux versus the temperature difference as shown in Fig. 17. At 1 bar inlet pressure and mass flux of 100 kg/m$^2$ s, the base heat flux was found to increase with increasing the temperature difference as a normal thermal trend. Both the micro pin fin and the multi-channels heat sinks provided higher base heat fluxes compared to the micro-gap heat sink due to the higher wall heat fluxes (heat transfer coefficients) and larger total heat transfer area. This figure also shows that the micro pin fin heat sink has higher base heat flux than that seen in the multi-channels heat sink because of the enhanced heat transfer process, as explained in the above sections. It can also be seen that around 350 kW/m$^2$ maximum base heat flux was reached in the micro pin fin heat sink due to the suppression of CHF in this geometry. Maximum base heat fluxes of 262 kW/m$^2$ and 184 kW/m$^2$ were found in the multi-channels and the micro-gap heat sinks, respectively.

### *3.4 Two-phase pressure drop*

The experimental two-phase pressure drop versus the exit vapour quality for each heat sink is presented in Fig. 18. For the micro-gap heat sink, this data covered a wall heat flux of 30–232 kW/m$^2$ and mass fluxes of 100, 150 and 200 kg/m$^2$ s, as shown in Fig. 18(a). For the multi-channels heat sink, Fig. 18(b) covered a wall heat flux of 8–308 kW/m$^2$ and mass flux of 100–300 kg/m$^2$ s. Fig. 18(c) depicts the experimental data of the micro pins heat sink for a wall heat flux of 18–324 kW/m$^2$ and mass flux of 100–250 kg/m$^2$ s. It can be seen that, for each heat sink, the two-phase pressure drop was found to increase with increasing exit vapour quality (heat flux). This could be due to the high bubble generation, coalescence rate and flow resistance when the heat flux is increased. In addition, increasing mass flux can lead to an increase in the two-phase pressure drop as a result of high wall shear stress.

The geometry effect on the two-phase pressure drop is shown in Fig. 19(a) at an inlet pressure of 1 bar and mass flux of 200 kg/m$^2$ s. This figure shows that, for a given exit quality, the micro pin fin heat exchanger had the highest two-phase pressure drop, with the lowest pressure drop reached in the micro-gap geometry. The micro-gap heat sink, as a plain and wide surface without flow disruption, is expected to provide lower wall shear stress and lower pressure drop. It is worth noting that, the maximum recorded two-phase pressure drop at this mass flux of 200 kg/m$^2$ s, was only around 13 kPa at an exit vapour quality of 0.95 using the micro pin fin heat sink. This pressure drop is considered small

compared to the total pressure drop across the entire thermal management system that will be required for cooling electronic components.

Fig. 19(b) is presented here to show the local total pressure (including single-phase and two-phase regions) along these heat sinks at a wall heat flux of 160 kW/m$^2$ and mass flux of 200 kg/m$^2$ s. It can be seen that the local total pressure decreased along the heated length. A small reduction can be seen in the single-phase region, while a clear reduction can be found during the two-phase region. A linear pressure drop with axial length was assumed in this calculation, hence the linear drop of the local pressure along the heated length. This assumption was discussed in Lee and Karayiannis [48]. This figure also depicts that, at these operating conditions, the micro pin fin heat sink had a pressure drop of 5.5 kPa compared to the multi-channels with 1.8 kPa pressure drop. The micro-gap heat sink showed the lowest pressure drop of 0.5 kPa.

From a design point of view, flow instability is considered a crucial challenge in using two-phase flow systems for electronics cooling. Flow reversal is commonly reported in the literature, especially in micro-scale configurations. This issue could affect the performance of any thermal management system. Therefore, the geometry effect on the boiling flow instability is presented in Fig. 19(c). This figure covers an inlet pressure of 1 bar, wall heat flux of 67 kW/m$^2$ and mass flux of 100 kg/m$^2$ s over a 10-second window. The signal fluctuation of the measured total pressure drop (in the entire heat sink), measured directly using a differential pressure transducer with an accuracy of ±0.07%, was used to assess this issue. The figure depicts that the fluctuation in the pressure drop signal of the micro pin fin heat sink was found to be only 0.07 kPa. The micro-gap also had low fluctuation of 0.08 kPa. In contrast, the multi-channels heat sink showed the largest pressure drop fluctuation of 0.52 kPa. This higher fluctuation in the pressure drop signal in the multi-channels could be due to the flow reversal that occurred in this geometry. This could be due to the confinement effect by the channel side-walls resulting also in an increased heat transfer rate to the vapour slugs and leading to expansion in both directions, i.e. towards the inlet and outlet. This phenomenon was discussed in detail in Al-Zaidi et al. [38] using rectangular multi-channels with the same working fluid. Back-flow or flow reversal was not seen in the micro-gap and the micro pin fin heat sinks leading to this low pressure drop fluctuation in these two geometries.

### *3.5 Pumping power required*

The abovementioned discussion showed that the micro pin fin geometry should be considered for moderate and high heat flux electronics instead of using the micro-gap or the multi-channels heat sinks. This is due to the following reasons; (i) the possibility of achieving higher heat fluxes without reaching the dryout region and CHF, (ii) reduction in instabilities and suppression of flow reversal and (iii) more uniform temperature distribution along the heat sink. The two-phase pressure drop introduced by these pins is higher than single-phase flows and the micro-gap and the multi-channels heat sink studied. However, the energy consumption of these two systems should be evaluated to clarify this point. Fig.

20 shows a comparison between the single-phase and the two-phase flow systems using the present micro pin fin heat sink. For the single-phase results, this figure was plotted at an inlet pressure of 1 bar and fluid temperature difference of 20 K, i.e. at fluid inlet and outlet temperature of 20 °C and 40 °C, respectively. In addition, the mass flux was varied up to 1098 kg/m$^2$ s to achieve the same dissipated heat transfer rates during the two-phase flow experiments. The two-phase flow operating conditions were carried out at 1 bar inlet pressure, 55 °C inlet fluid temperature (5 K degree of subcooling) and mass flux of 250 kg/m$^2$ s. The supplied heat was increased until the exit vapour quality of one was reached. Fig. 20(a) depicts that both single-phase and two-phase pressure drop increased with increasing required cooling capacity. This is due to the fact that higher mass flow rates (high wall shear stress) are required in the single-phase flow with increasing cooling capacity. In the two-phase flow system, at a given mass flux, the two-phase pressure drop components increased with increasing heat transfer rates as a result of flow resistance. This figure also shows that, for a given cooling capacity, the two-phase pressure drop was much higher than the single-phase pressure drop as expected. This became more noticeable with increasing cooling capacity. For example, at a maximum cooling capacity of 315 W, the pressure drop of the micro pin fin heat sink was found to be 11 kPa for the single-phase and 18 kPa for the two-phase, i.e. an increase of 64%. However, a different trend can be seen when the pumping power versus the cooling capacity is plotted in Fig. 20 (b). Generally, the energy consumption by the pump to meet this load was determined to be relatively small, i.e. less than 0.14 W. This is because only the pressure drop across the pins geometry was considered here, and higher pumping power is expected when the entire thermal management system is included. It can also be seen that the pumping power increased with the cooling capacity as a result of high pressure drop in both systems. At a cooling capacity lower than 150 W, the two-phase flow system showed slightly higher pumping power than that in the single-phase flow. In contrast, when the cooling capacity increased above 150 W, the two-phase flow system consumed lower energy compared to the single-phase flow. Higher mass flow rates should be required in the single-phase flow compared to the two-phase flow in order to achieve the same cooling capacity. In other words, the pumped two-phase flow system consumes lower power for the same cooling capacity due to the lower mass flow rates as a result of phase-change.

For most electronics, the thermal design power generated by chipsets can be equal or more than 150 W. For example, the most recent Intel Core Ultra 7 processor (270 K Plus) can generate a TDP of 250 W at maximum turbo power (highest power consumption of the processor) [49]. The present comparison shows that, at this TDP, the pumping power required in the single-phase flow was found to be two times higher than that in the two-phase flow system as shown in Fig. 20(b). It is interesting to know that CPU Water Coolers are widely used to cool down this generated thermal power. However, using water as a coolant can result in a number of issues such as: (i) corrosion, (ii) contamination, (iii) high electrical conductivity (leakage and then short-circuit fault), (iv) freezing expansion, and (v) non-uniform temperature distribution. The present pumped two-phase flow system with micro pin fin geometry shows a potential thermal performance and can be safely used. The average surface

temperature reported in this figure was lower than 90 °C, which is within the acceptable range of this CPU, i.e. 105 °C at maximum operating temperature [49]. This design can be scaled for large cooling applications, such as data centres, to handle high thermal loads while reducing total energy consumption and carbon footprint.

## 4. Conclusions

Two-phase flow of HFE-7100 in three different heat sink geometries was experimentally tested at a system pressure of 1 bar, inlet subcooling of 5 K, mass flux of 100–300 kg/m$^2$ s and wall heat flux up to 0.324 MW/m$^2$. Micro-gap, multi-channels and micro pin fin heat sinks were examined in this study. A high-speed camera was used to study the effect of different parameters on the flow boiling patterns. The following findings can be summarised:

Different flow regimes were visualised at different operating conditions. These flow regimes were also found to vary in the three examined geometries. The flow regimes in the micro-gap geometry were bubbly, mixed and vapour layer-liquid straps flow. In the micro-channels heat sink four different flow regimes were observed, namely: bubbly, slug, churn and annular flow. In the micro pin fin heat exchanger three flow regimes can be identified: bubbly, mixed and vapour layer flow. It was observed that the wall-edges of the channels or the pins can promote a higher number of nucleation sites compared to the simple micro-gap geometry. In addition, the surface feed marks (surface microstructures introduced by the cutting tools) can also enhance nucleation. Flow reversal was observed in the multi-channels, and a zig-zag flow without back-flow was visualised in the micro-gap and the micro pins heat sinks.

The heat transfer coefficient increased with increasing wall heat flux, with the micro pin fin geometry providing higher heat transfer coefficients compared to the other two geometries. Dryout and then the critical heat flux were found to occur in the micro-gap and the multi-channels heat sinks at lower temperature differences compared to the micro pin fin heat sink. The CHF flux was 232 kW/m$^2$ and 308 kW/m$^2$ for the micro-gap and the multi-channels heat sink for the range studied. The micro pin fin heat sink can operate at higher heat flux values, i.e. CHF was not reached in the present range.

The mass flux effect on the boiling curve was insignificant in the examined ranges. However, it is worth noting the higher mass flux can allow the heat sinks to operate at higher heat fluxes before reaching critical heat flux, hence it can be considered a critical parameter in system design.

The resulting temperature distribution of the surface to be cooled, i.e. electronic chip in this case, is important along with the actual resulting temperature at a given thermal load. It was concluded that the micro pin fin geometry can provide the lowest surface temperature with less variation between the inlet and outlet of the heat sink.

Higher two-phase pressure drop was recorded in the micro pins heat sink compared to the micro-gap and the multi-channels heat sinks. However, this is a small component of the total pressure drop in the thermal management system. In addition, the experimental analysis of energy consumption using this

geometry showed that the pumped two-phase flow system consumed less energy than the single-phase flow system in achieving the same cooling loads.

**Acknowledgements**

The work was conducted with the support of the Engineering and Physical Sciences Research Council of the UK, under Grant: EP/T033045/1.

## Nomenclature

| | |
|---|---|
| $A$ | Area ($m^2$) |
| $cp$ | Specific heat capacity (J/kg K) |
| $D_h$ | Hydraulic diameter (m) |
| $f$ | Friction factor (-) |
| $G$ | Mass flux (kg/m² s) |
| $h$ | Heat transfer coefficient (W/$m^2$ K) |
| $\bar{h}$ | Average heat transfer coefficient (W/$m^2$ K) |
| $H$ | Height (m) |
| $i$ | Specific enthalpy (J/kg) |
| $i_{lg}$ | Latent heat of vapourisation (J/kg) |
| $k$ | Thermal conductivity (W/m K) |
| $L$ | Length (m) |
| $m$ | Fin parameter, see Eq. (12) (-) |
| $\dot{m}$ | Mass flow rate (kg/s) |
| $n$ | Number of data points (-) |
| $N_{ch}$ | Number of channels (-) |
| $N_{pin}$ | Number of pins (-) |
| $Nu$ | Average Nusselt number (-), $Nu = \bar{h}D_h/k_l$ |
| $P$ | Pressure (Pa) |
| $Q_{cc}$ | Cooling capacity (W) |
| $Q_p$ | Pump power (W) |
| $q''$ | Heat flux (W/m²) |
| $Ra$ | Average surface roughness (µm) |
| $Sa$ | Average surface roughness of scanned area (µm) |
| $S_D$ | Diagonal pitch (m) |
| $S_L$ | Longitudinal pitch [m) |
| $S_T$ | Transverse pitch (m) |
| $T$ | Temperature (K) |
| $\bar{T}$ | Average temperature (K) |
| $U$ | Absolute uncertainty (-) |
| $W$ | Width (m) |
| $x$ | Vapour quality (-) |
| $y$ | Vertical distance between first row of thermocouples and surface bottom (m) |
| $z$ | Distance measured from inlet to end of heated length (m) |
| $\sigma(\Delta P)$ | Standard deviation of experimental pressure drop (Pa) |

Greek Symbols

| | |
|---|---|
| $\Delta P$ | Pressure drop (Pa) |
| $\Delta T$ | Temperature difference (K) |
| $\eta$ | Efficiency (-) |
| $\rho$ | Density (kg/m³) |

Subscripts

| | |
|---|---|
| *b* | Base |
| *ch* | Channel |
| *cu* | Copper |
| *f* | Fin |
| *ht* | Heat transfer |
| *in* | Inlet |
| *l* | Liquid |
| *meas* | Measured |
| *p* | Pump |
| *sat* | Saturation |
| *sc* | Sudden contraction |
| *se* | Sudden expansion |
| *sp* | Single-phase |
| *sub* | Sub-cooled |
| *th* | Thermocouple |
| *tp* | Two-phase |
| *w* | Wall |
| *z* | Axial location |

Abbreviations

| | |
|---|---|
| *CHF* | Critical heat flux (W/m$^2$) |
| *MAE* | Mean absolute error (-) |
| *ONB* | Onset of nucleate boiling (-) |
| *PP* | Pumping power (W) |
| *TDP* | Thermal design power (W) |
| *VCC* | Vapour compression cycle (-) |

**References**


[1] L. Narayan, “Thermal Management Market Companies, Size & Trends 2026-2035” Precedence Research, report code: 3449 (Energy and Power). https://www.precedenceresearch.com/thermal-management-market (accessed October 02, 2026).

[2] T. G. Karayiannis and M. M. Mahmoud, “Flow boiling in microchannels: Fundamentals and applications,” *Appl. Therm. Eng.*, vol. 115, pp. 1372–1397, 2017.

[3] A. Fly, “Thermal and water management of evaporatively cooled fuel cell vehicles,” Loughborough University (PhD thesis), 2015.

[4] J. Jörg, S. Taraborrelli, G. Sarriegui, R. W. De Doncker, R. Kneer, and W. Rohlfs, “Direct single impinging jet cooling of a MOSFET power electronic module,” *IEEE Trans. Power Electron.*, vol. 33, no. 5, pp. 4224–4237, 2017.

[5] P. Narsai, E. Momanyi, K. Venkataraman, B. Evans, and B. J. Cantwell, “Indirect heat flux measurements at the nozzle throat of a hybrid rocket motor,” in *In 51st AIAA/SAE/ASEE Joint Propulsion Conference*, 2015.

[6] P. Norajitra, L. V Boccaccini, T. Ihli, G. Janeschitz, P. Karditsas, and W. Krauss, “Development of He-cooled divertors for fusion power plants,” *Fusion Eng. Des.*, vol. 82, no. 15, pp. 2740–2744, 2007.

[7] J. S. Park, D. Shin, S. Yim, and S. Kim, “Evaluate the cooling performance of transmit / receive module cooling system in active electronically scanned array radar,” *Electronics*, vol. 10, p. 1044, 2021.

[8] S. K. Roy and B. L. Avanic, “A very high heat flux microchannel heat exchanger for cooling of semiconductor laser diode arrays,” *IEEE Trans. Components Packag. Manuf. Technol. Part B*, vol. 19, no. 2, pp. 444–451, 1996.

[9] S. Wang, J. Shi, H. H. Chen, S. R. Schafer, M. Munir, G. Stecker, W. Pan, J. J. Lee, and C. L. Chen, “Cooling design and evaluation for photovoltaic cells within constrained space in a CPV/CSP hybrid solar system,” *Appl. Therm. Eng.*, vol. 110, pp. 369–381, 2017.

[10] G. Kopp, “Solar irradiance measurements,” *Living Rev. Sol. Phys.*, vol. 22, no. 1, pp. 1–102, 2025.

[11] M. K. Sung and I. Mudawar, “CHF determination for high-heat flux phase change cooling system incorporating both micro-channel flow and jet impingement,” *Int. J. Heat Mass Transf.*, vol. 52, no. 3–4, pp. 610–619, 2009.

[12] X. Yu, C. Woodcock, Y. Wang, J. Plawsky, and Y. Peles, “Enhanced Subcooled Flow Boiling Heat Transfer in Microchannel with Piranha Pin Fin,” *ASME J. Heat Transf.*, vol. 139, no. 11, pp. 1–13, 2017.

[13] L. Xiang, X. Yu, T. Hong, X. Yang, B. Xie, R. Hu, and X. Luo, “Performance of spray cooling with vertical surface orientation: An experimental investigation,” *Appl. Therm. Eng.*, vol. 219, p. 119434, 2023.

[14] E. G. Colgan, B. Furman, M. Gaynes, N. LaBianca, J. Magerlein, R. Polastre, R. J. Bezama, R. Choudhary, K. Marston, H. Toy, J. A. Wakil, and R. Schmidt, “Silicon microchannel cooling for high power chips,” *HVAC R Res.*, vol. 12, no. 4, pp. 1031–1045, 2006.

[15] M. Fabbri and V. K. Dhir, “Optimized heat transfer for high power electronic cooling using arrays of microjets,” *ASME*, vol. 127, no. 7, pp. 760–769, 2005.

[16] B. Agostini, J. R. Thome, M. Fabbri, and B. Michel, “High heat flux two-phase cooling in silicon multimicrochannels,” *IEEE Trans. Components Packag. Technol.*, vol. 31, no. 3, pp. 691–701, 2008.

[17] Z. F. Zhou, X. W. Lin, R. J. Ji, D. Q. Zhu, B. Chen, H. Wang, and Y. J. Lu, “Enhancement of

heat transfer on micro- and macro- structural surfaces in close-loop R410A flashing spray cooling system for heat dissipation of high-power electronics," *Appl. Therm. Eng.*, vol. 223, p. 119978, 2023.

[18] H. Lim, S. Y. Doh, D. H. Shin, S. M. You, and J. Lee, "Thermal performance of a boiling-driven heat spreader using passive flow control," *Case Stud. Therm. Eng.*, vol. 41, p. 102604 Contents, 2023.

[19] J. Li, D. Wang, and G. P. Peterson, "Experimental studies on a high performance compact loop heat pipe with a square flat evaporator," *Appl. Therm. Eng.*, vol. 30, no. 6–7, pp. 741–752, 2010.

[20] J. J. Wei and H. Honda, "Effects of fin geometry on boiling heat transfer from silicon chips with micro-pin-fins immersed in FC-72," *Int. J. Heat Mass Transf.*, vol. 46, no. 21, pp. 4059–4070, 2003.

[21] A. Poachaiyapoom, R. Leardkun, and J. Mounkong, "Miniature vapor compression refrigeration system for electronics cooling," *Case Stud. Therm. Eng.*, vol. 13, p. 100365, 2019.

[22] W. G. Anderson, P. M. Dussinger, D. B. Sarraf, and S. Tamanna, "Heat pipe cooling of concentrating photovoltaic cells," in *33rd IEEE Photovoltaic Specialists Conference*, 2008, pp. 1–6.

[23] B. Cong, Y. Kong, Y. Ye, R. Liu, X. Du, L. Yu, S. Jia, Z. Qu, and B. Jiao, "A combined solution of thermoelectric coolers and microchannels for multi-chip heat dissipation with precise temperature uniformity control," *Appl. Therm. Eng.*, vol. 219, p. 119370, 2023.

[24] Y. Cai, B. H. Hong, W. X. Wu, W. W. Wang, and F. Y. Zhao, "Active cooling performance of a PCM-based thermoelectric device: Dynamic characteristics and parametric investigations," *Energy*, vol. 254, p. 124356, 2022.

[25] Meech, "Air Technology Vortex Cooling Range: Effective Industrial Cooling," 2018. [Online]. Available: www.meech.com

[26] M. Saini and R. L. Webb, "Heat rejection limits of air cooled plane fin heat sinks for computer cooling," in *Eighth Intersociety Conference on Thermal and Thermomechanical Phenomena in Electronic Systems, ITHERM*, 2002, pp. 1–8.

[27] H. Goshayeshi, M. Fahiminia, and M. M. Naserian, "Improvement of free convection heat transfer rate of rectangular heat sink on vertical base plates," *Energy Power Eng.*, vol. 3, no. 4, pp. 525–532, 2011.

[28] Z. Li, X. Zhao, Y. Shen, M. Zhang, Y. Zhao, and K. Liang, "Boiling heat transfer enhancement and pressure drop analysis of Novec-649 in microchannel pin- fin heat sinks," *Exp. Heat Transf. Taylor Fr. Gr.*, pp. 1–18, 2026.

[29] Q. Tao, B. Liu, Q. Li, S. Hong, and Z. Wu, "Experimental study of the flow boiling heat transfer characteristics of micro-pin-fin microcavity surface in semiopen microchannel," *SSRN*, no. 6880444, 2026.

[30] K. Huang, L. Guiping, G. Yuandong, T. Kai, H. Jinyin, Z. Hongxing, M. Jianyin, "Visualization experimental study on two-phase flow boiling characteristics in leaf vein manifold microchannel heat sinks," *Int. J. Therm. Sci.*, vol. 223, p. 110604, 2026.

[31] W. R. Chang, C. A. Chen, J. H. Ke, and T. F. Lin, "Subcooled flow boiling heat transfer and associated bubble characteristics of FC-72 on a heated micro-pin-finned silicon chip," *Int. J. Heat Mass Transf.*, vol. 53, pp. 5605–5621, 2010.

[32] D. A. McNeil, A. H. Raeisi, P. A. Kew, and P. R. Bobbili, "A comparison of flow boiling heat-transfer in in-line mini pin fin and plane channel flows," *Appl. Therm. Eng.*, vol. 30, no. 16, pp. 2412–2425, 2010.

[33] M. Law and P. S. Lee, "A comparative study of experimental flow boiling heat transfer and pressure characteristics in straight- and oblique-finned microchannels," *Int. J. Heat Mass Transf.*, vol. 85, pp. 797–810, 2015.

[34] B. Markal, B. Kul, M. Avci, and R. Varol, “Effect of gradually expanding flow passages on flow boiling of micro pin fin heat sinks,” *Int. J. Heat Mass Transf.*, vol. 197, p. 123355, 2022.

[35] A. P. Moreira, A. G. da S. Vilaronga, J. D. de Oliveira, and E. M. Cardoso, “Heat Transfer and Two-Phase Flow of Deionized Water in Heat Sink With Micro-Pin Fins,” *Results Eng.*, vol. 27, p. 106378, 2025.

[36] Y. Xie, Z. Dong, X. Li, C. Lu, X. Zhuang, and P. Yu, “Experimental study on flow boiling heat transfer and pressure drop characteristics of HFE-7100 in different structured microchannels,” *Int. Commun. Heat Mass Transf.*, vol. 179, no. P1, p. 112164, 2026.

[37] H. Yu, C. Pei, X. Tang, A. Hong, Q. Xu, and L. Guo, “Enhanced flow boiling heat transfer in manifold pin-fin microchannel heat sink,” *Appl. Therm. Eng.*, vol. 302, 2026.

[38] A. H. Al-Zaidi, M. M. Mahmoud, and T. G. Karayiannis, “Flow boiling of HFE-7100 in microchannels: Experimental study and comparison with correlations,” *Int. J. Heat Mass Transf.*, vol. 140, pp. 100–128, 2019.

[39] A. H. Al-Zaidi, M. M. Mahmoud, and T. G. Karayiannis, “Flow boiling in copper and aluminium microchannels,” *Int. J. Heat Mass Transf.*, vol. 194, p. 123101, 2022.

[40] A. H. Al-Zaidi and T. G. Karayiannis, “Flow boiling in micro-pin fin heat exchangers and comparison with correlations,” *Appl. Therm. Eng.*, vol. 283, p. 129008, 2026.

[41] A. H. Al-Zaidi, M. M. Mahmoud, A. Ivanov, and T. G. Karayiannis, “Bubble nucleation site density, generation frequency and departure diameter in flow boiling of HFE-7100,” *Int. J. Heat Mass Transf.*, vol. 242, p. 126830, 2025.

[42] H. W. Coleman and W. G. Steele, *Experimentation and uncertainty analysis for engineers*, 3nd ed. New York: Wiley, Chichester, 2009.

[43] R. K. Shah and A. L. London, *Laminar flow forced convection in ducts, Supplement 1 to Advances in Heat Transfer*. Academic Press New York, 1978.

[44] D. Copeland, “Optimization of parallel plate heatsinks for forced convection,” *Sixt. Annu. IEEE Semicond. Therm. Meas. Manag. Symp. IEEE*, pp. 266–272, 2000.

[45] P. X. Jiang, M. H. Fan, G. S. Si, and Z. P. Ren, “Thermal Hydraulic Performance of Small Scale Micro-Channel and Porous-Media Heat Exchangers,” *Int. J. Heat Mass Transf.*, vol. 44, pp. 1039–1051, 2001.

[46] P. S. Lee and S. V. Garimella, “Thermally developing flow and heat transfer in rectangular microchannels of different aspect ratios,” *Int. J. Heat Mass Transf.*, vol. 49, no. 17–18, pp. 3060–3067, 2006.

[47] A. Kosar and Y. Peles, “Boiling heat transfer in a hydrofoil-based micro pin fin heat sink,” *Int. J. Heat Mass Transf.*, vol. 50, pp. 1018–1034, 2007.

[48] V. Y. S. Lee and T. G. Karayiannis, “Effect of Inlet Subcooling on Flow Boiling in Microchannels,” *Appl. Therm. Eng.*, vol. 181, p. 115966, 2020.

[49] Intel, “Intel Core Ultra 7 processor 270K Plus,” 2026. https://www.intel.com/content/www/us/en/products/sku/245692/intel-core-ultra-7-processor-270k-plus-36m-cache-up-to-5-50-ghz/specifications.html (accessed March 16, 2026).

**List of tables**

**Table 1** Dimensions and surface roughness measurements of the present heat sinks, see Fig. 5(c).

| Symbol | Unit | Micro-gap | Multi-channels | Micro Pins |
|---|---|---|---|---|
| $W_b$ | mm | 20 | 20 | 20 |
| $L_b$ | mm | 25 | 25 | 25 |
| $H_{ch}$ or $H_{pin}$ | mm | 1 | 1 | 1 |
| $W_{ch}$ | mm | 20 | 0.95 | --- |
| $W_f$ | mm | --- | 0.6 | 0.6 |
| $S_T$ | mm | --- | --- | 2.19 |
| $S_L$ | mm | --- | --- | 1.095 |
| $S_D$ | mm | --- | --- | 1.55 |
| $D_h$ | mm | 1.9 | 0.97 | 1.14 |
| $N_{ch}$ or $N_{pin}$ | - | 1 | 13 | 207 |
| $A_{ht}$ | $m^2$ | 0.00055 | 0.00096 | 0.00097 |
| $R_a$ | μm | 0.122 | 0.102 | 0.151 |
| $S_a$ | μm | 0.132 | 0.103 | 0.114 |

**Table 2** Experimental uncertainties.

| Variables | Uncertainty |
|---|---|
| Temperature | ±0.21−0.6 K |
| Pressure | ±0.25% |
| Mass flow rate | ±0.035% |
| Fanning friction factor | up to ±4.7% |
| Reynolds number | ±0.28–0.4% |
| Average Nusselt number | ±11–16% |
| Wall heat flux | up to ±17% |
| Average two-phase heat transfer coefficient | up to ±16% |

**List of figures**

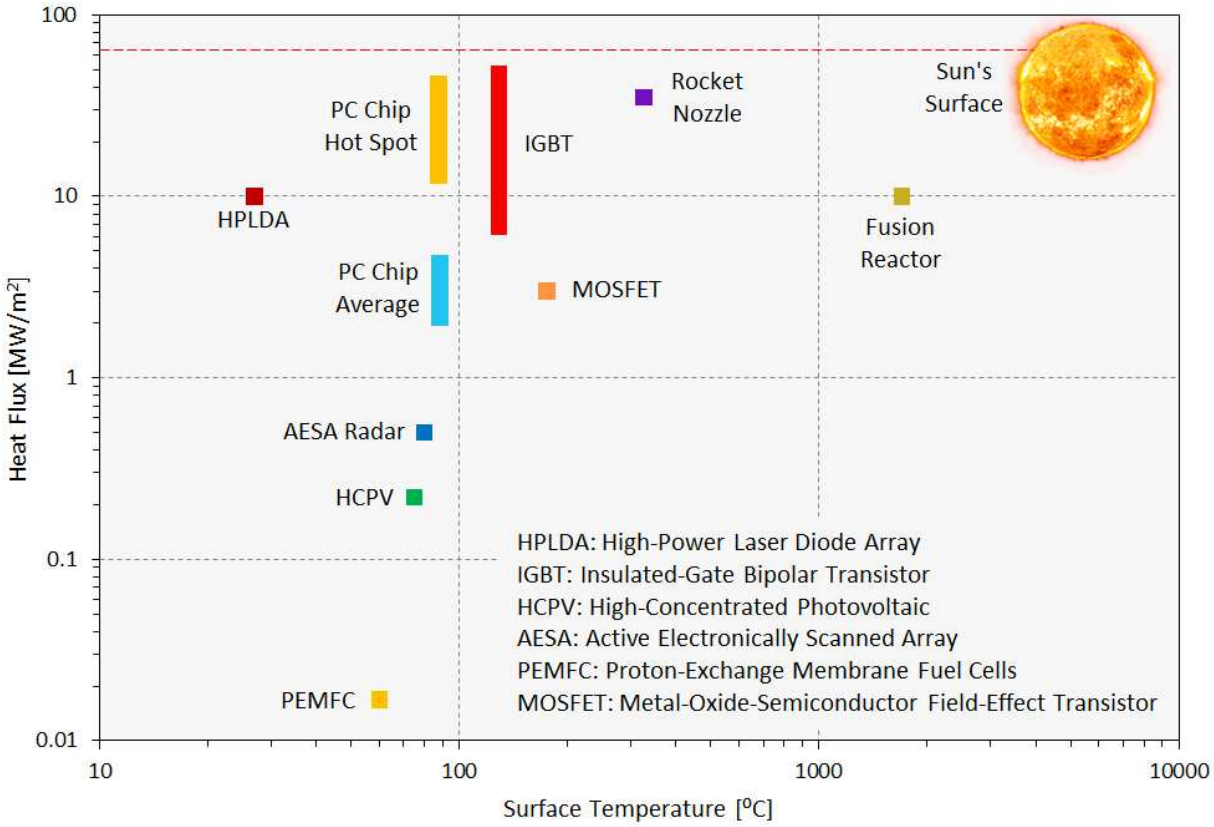



**Fig. 1** Thermal operating conditions of different applications.
(sun image source: solarsystemscope.com)

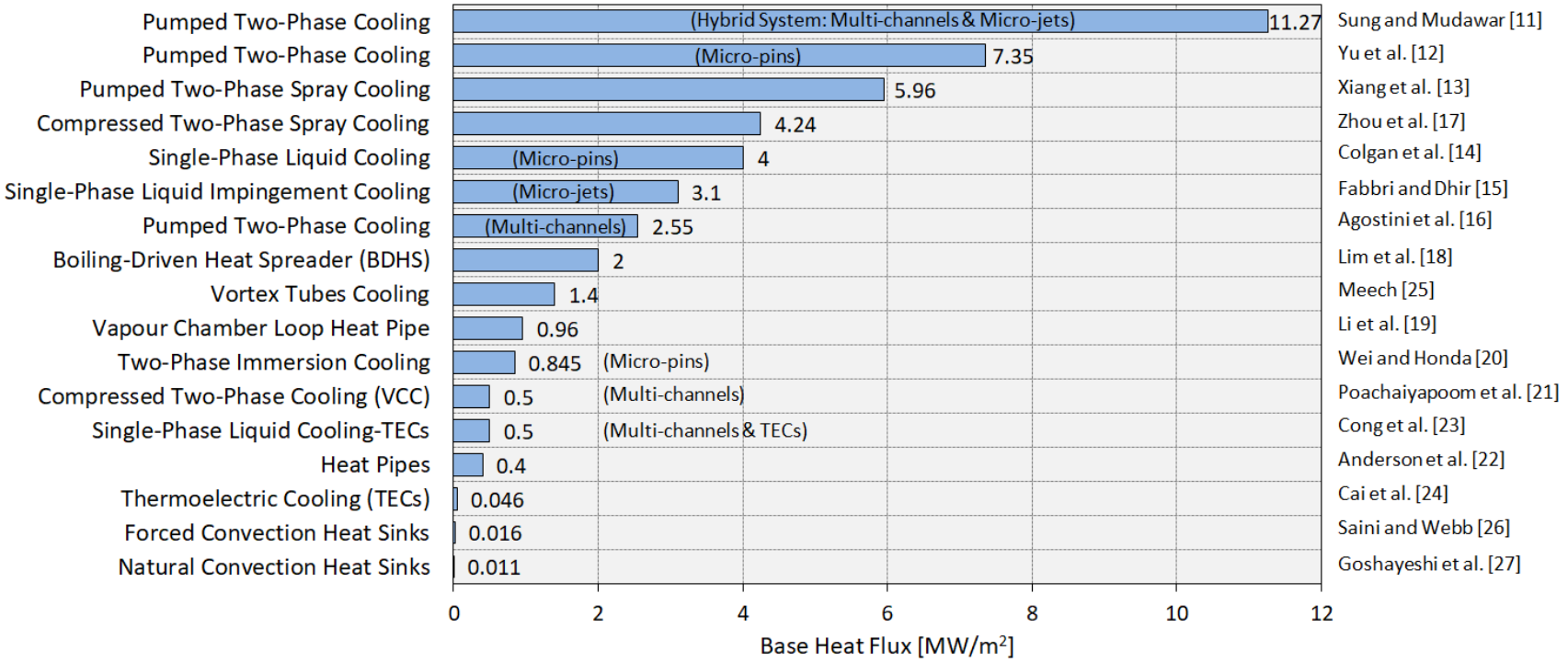



**Fig. 2** Thermal limits of different thermal management solutions for electronics (existing and under development).

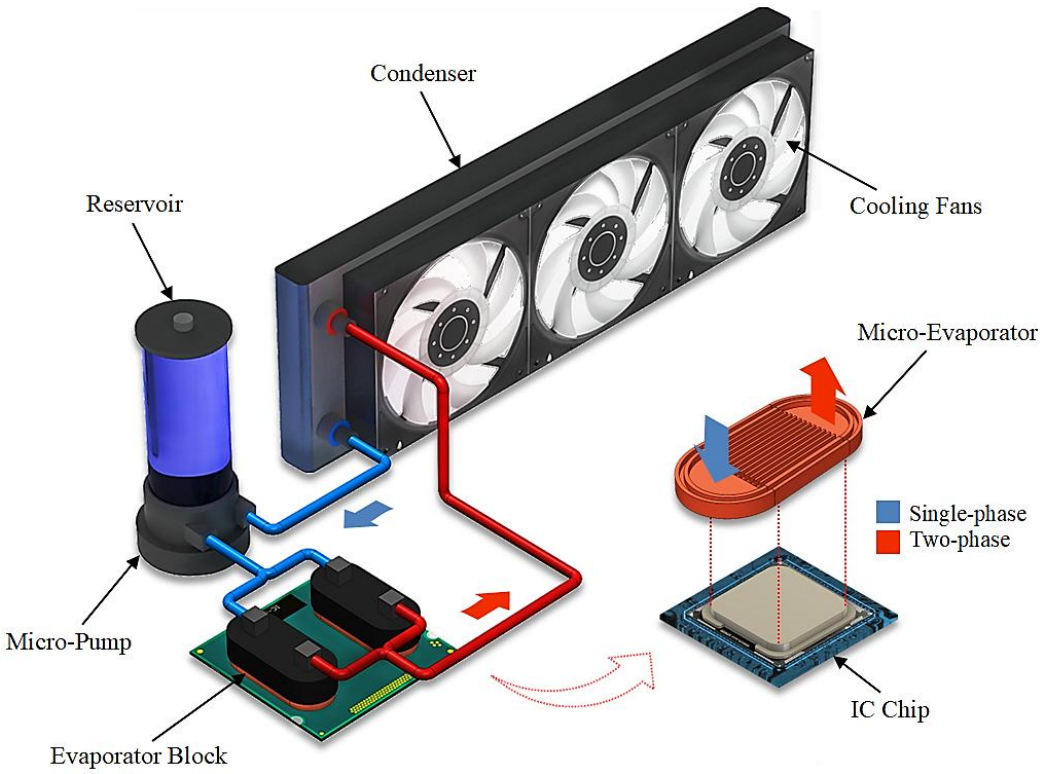



**Fig. 3** Schematic diagram of multiple micro-evaporators pumped two-phase flow system for electronics (not to scale).

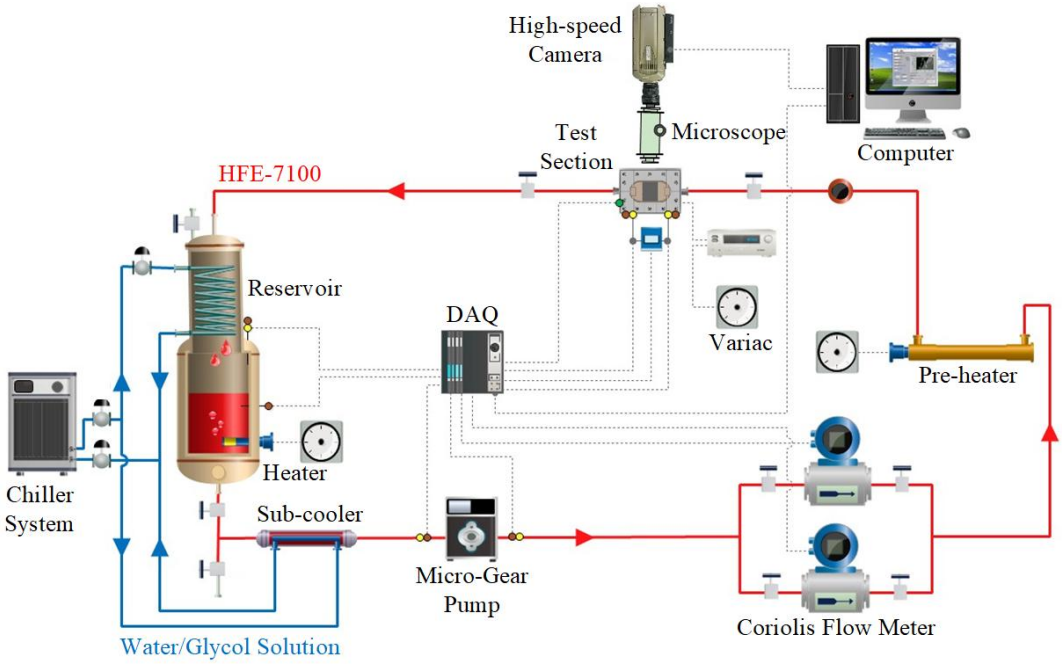



**Fig. 4** Present experimental facility, [38].

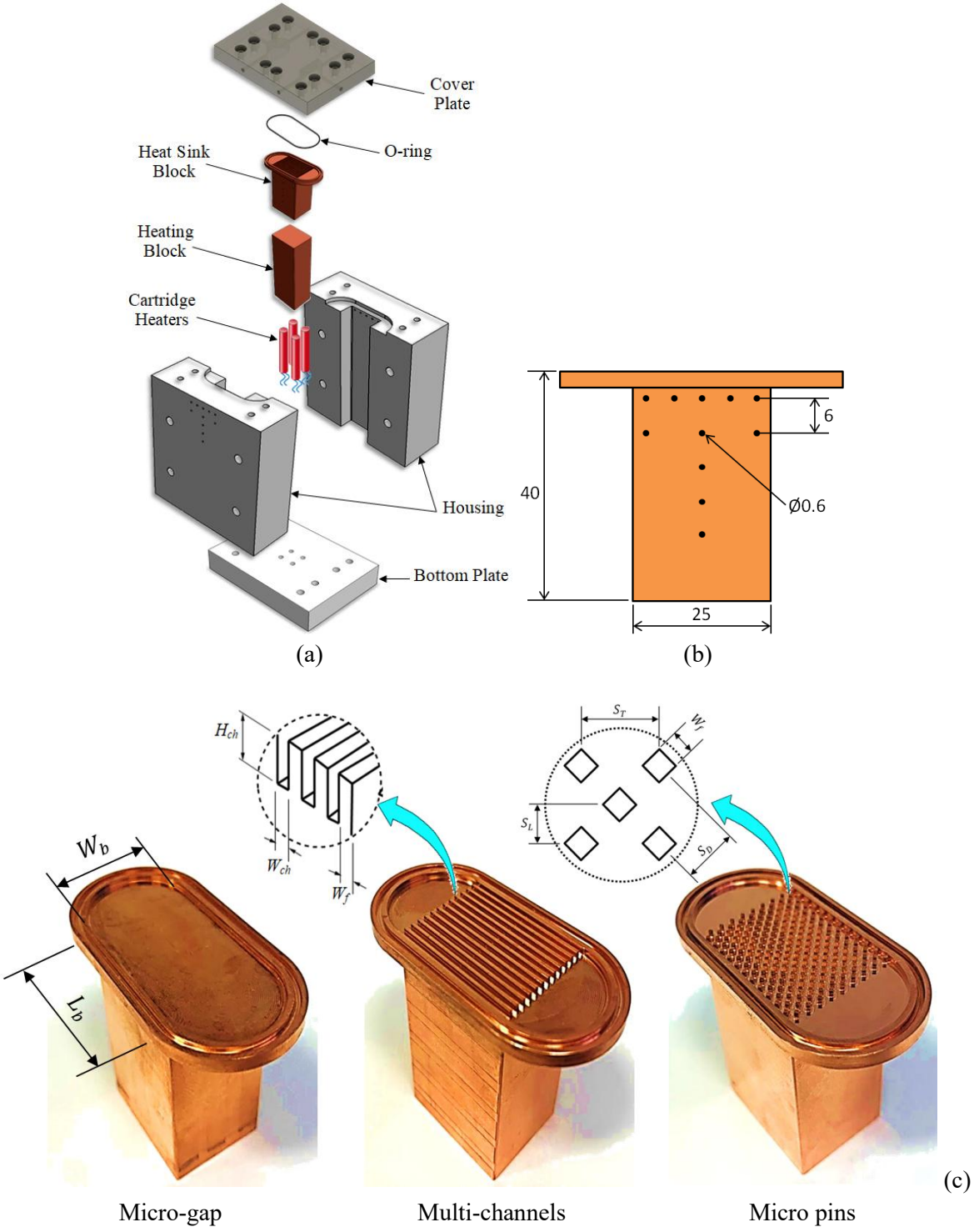
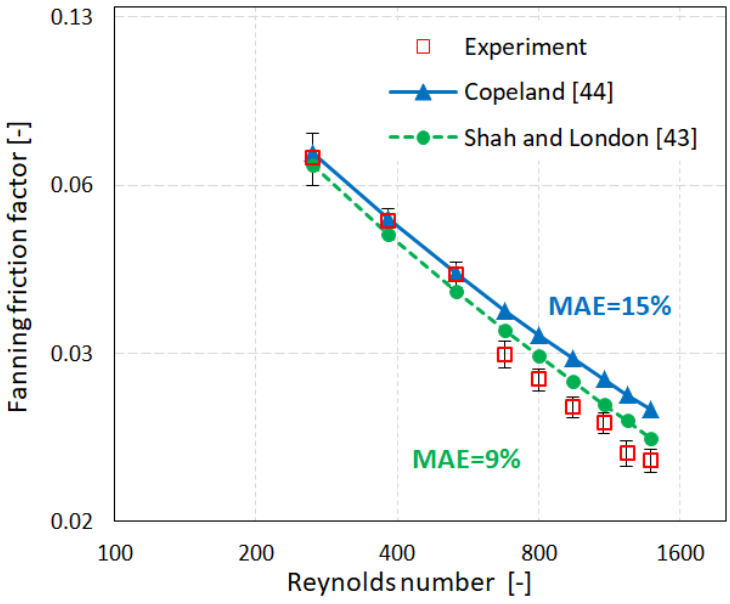
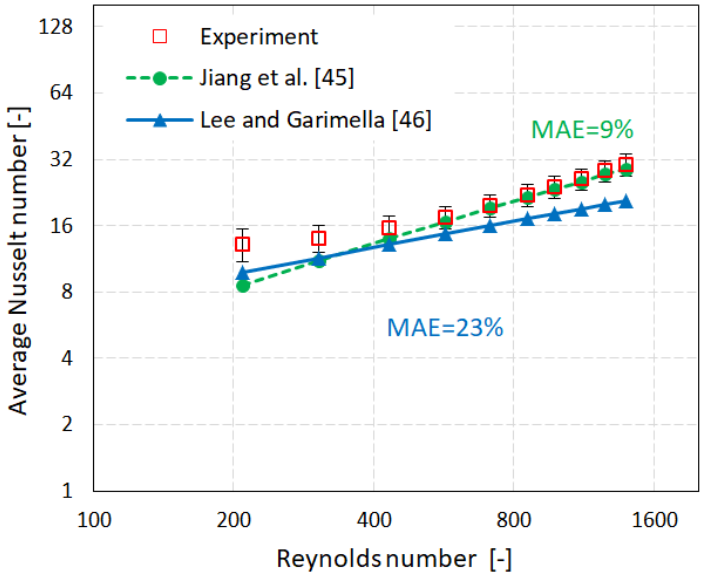



**Fig. 5** Present test section:

(a) Exploded drawing, [40] (b) Heat sink dimensions in [mm] (c) Photograph of three heat sinks.




(a)




(b)

**Fig. 6** Validation results for the multi-channels:

(a) Fanning friction factor (b) Average Nusselt number.

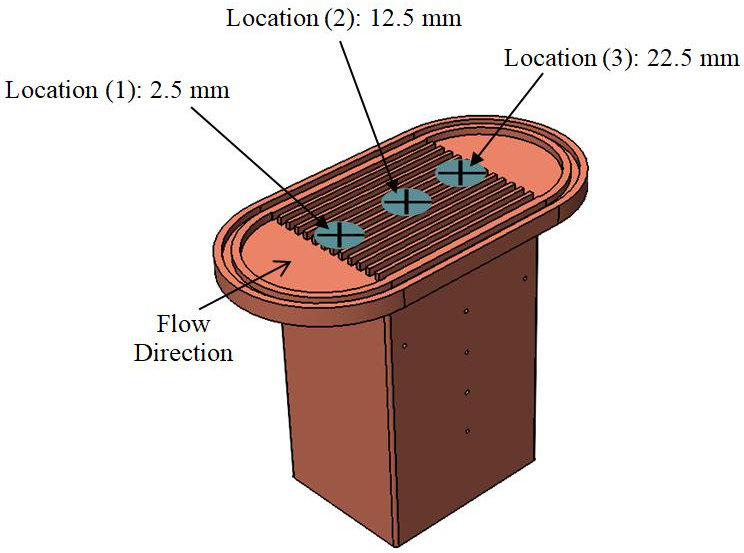
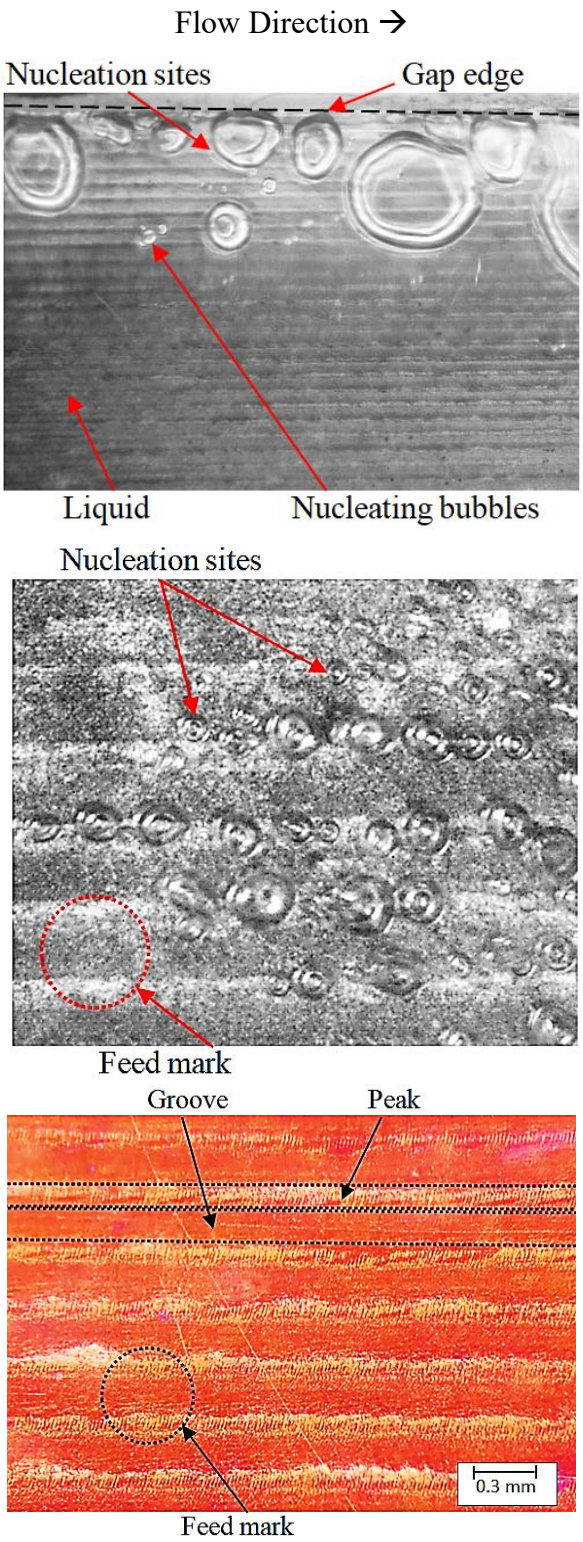



**Fig. 7** Locations of flow visualisation measured from channel inlet.




(a)
$q''_w$: 39 kW/m$^2$

(b)
$q''_w$: 58.6 kW/m$^2$

(c)
Microscope image:
3X magnification

**Fig. 8** Effect of wall heat flux at inlet pressure of 1 bar, mass flux of 100 kg/m$^2$ s and location (1), for the micro-gap.

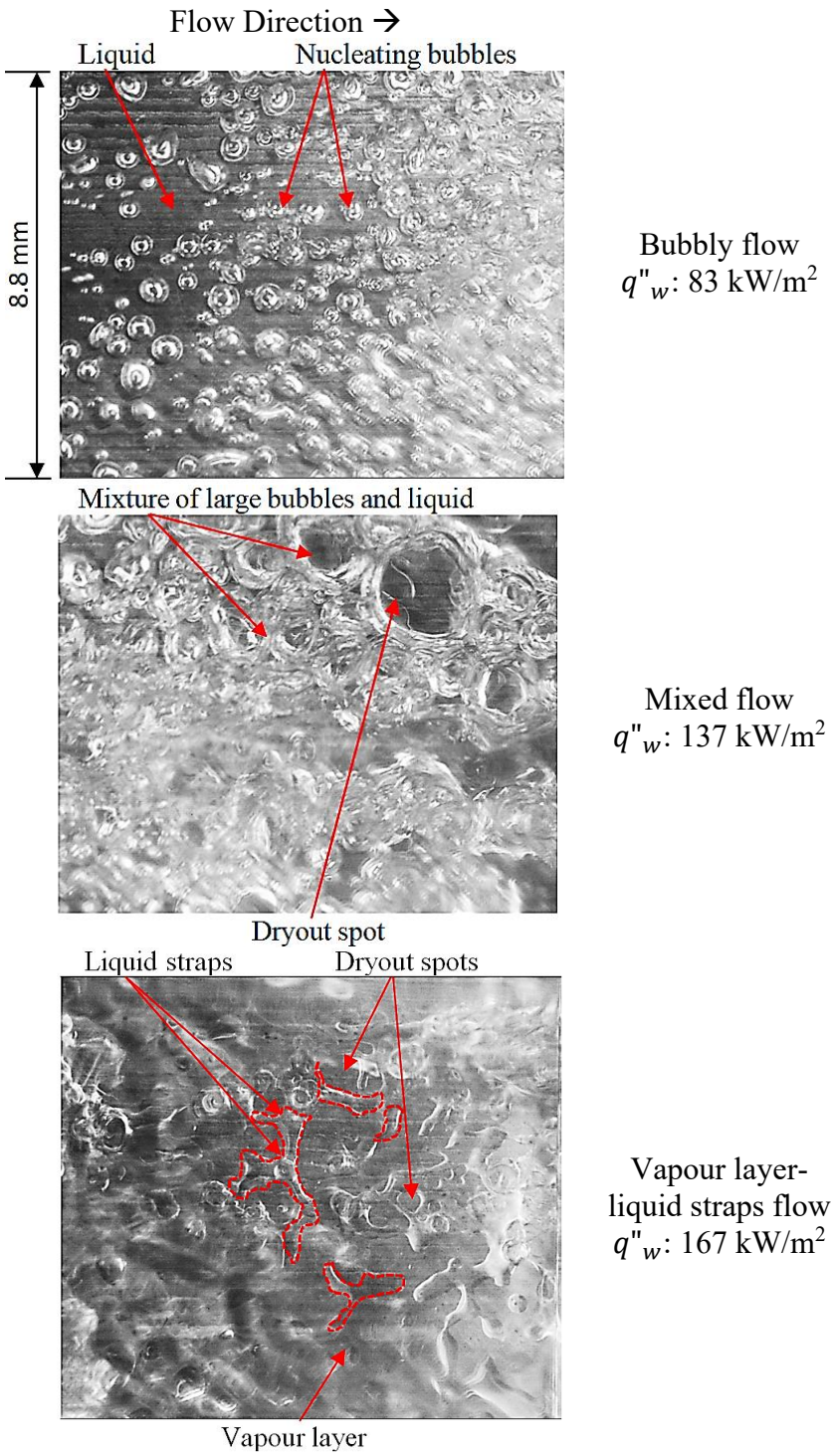



**Fig. 9** Effect of wall heat flux at inlet pressure of 1 bar, mass flux of 100 kg/m$^2$ s and location (2), for the micro-gap.

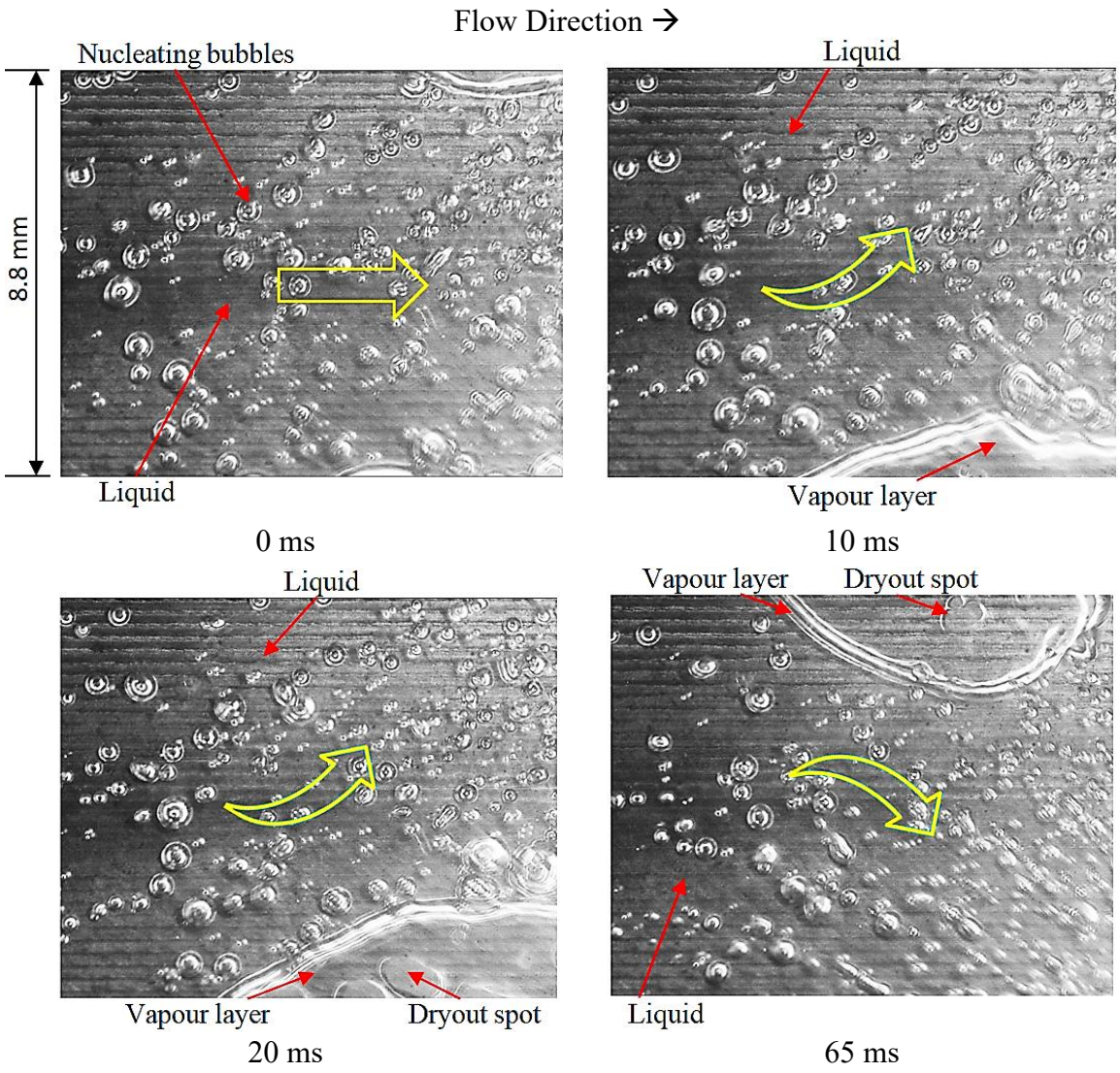



**Fig. 10** Zig-zag flow at inlet pressure of 1 bar, mass flux of 100 kg/m$^2$ s, wall heat flux 72 kW/m$^2$ and location (1), for the micro-gap.

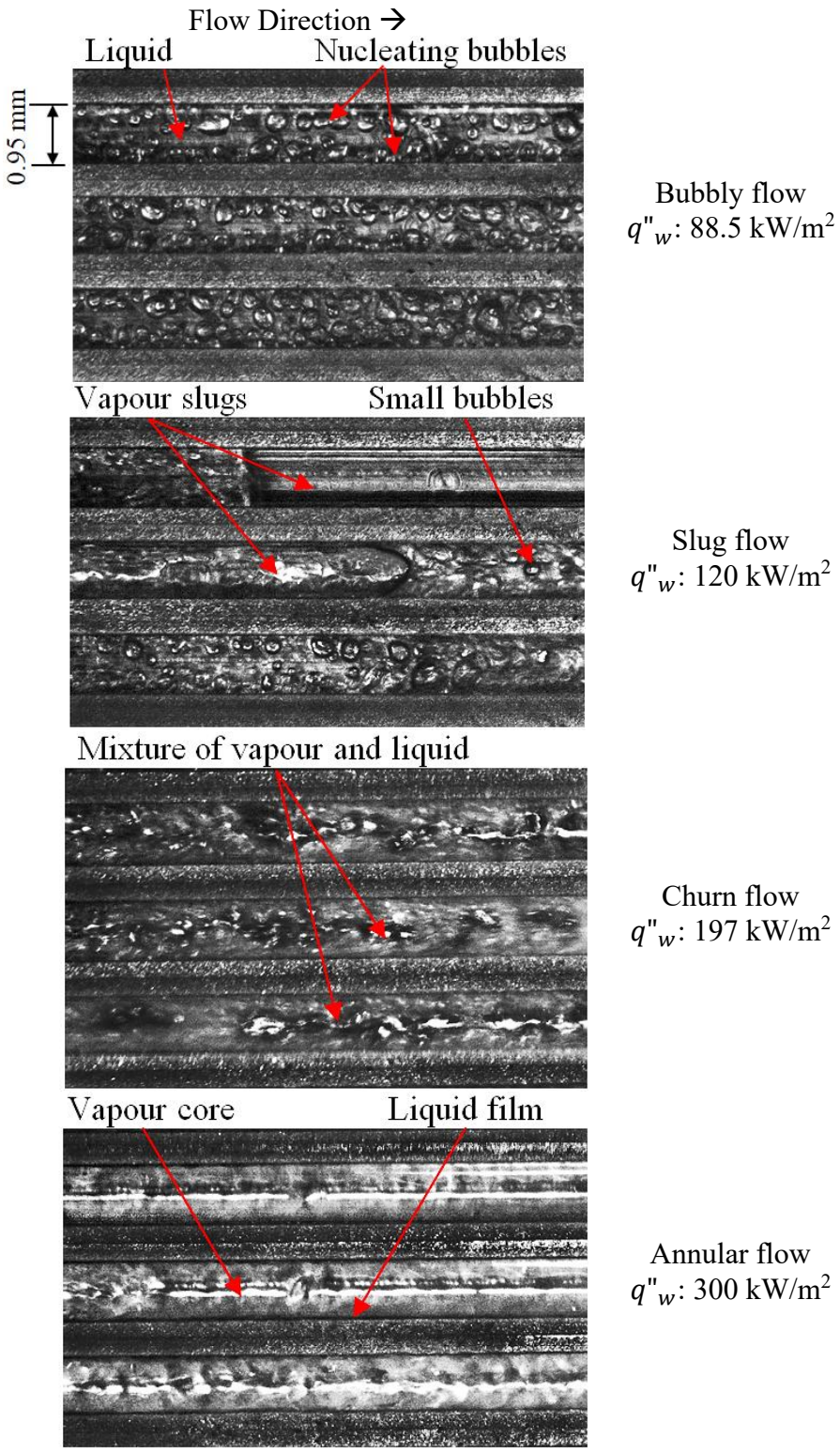



**Fig. 11** Effect of wall heat flux at inlet pressure of 1 bar, mass flux of 300 kg/m$^2$ s and location (2), for the multi-channels.

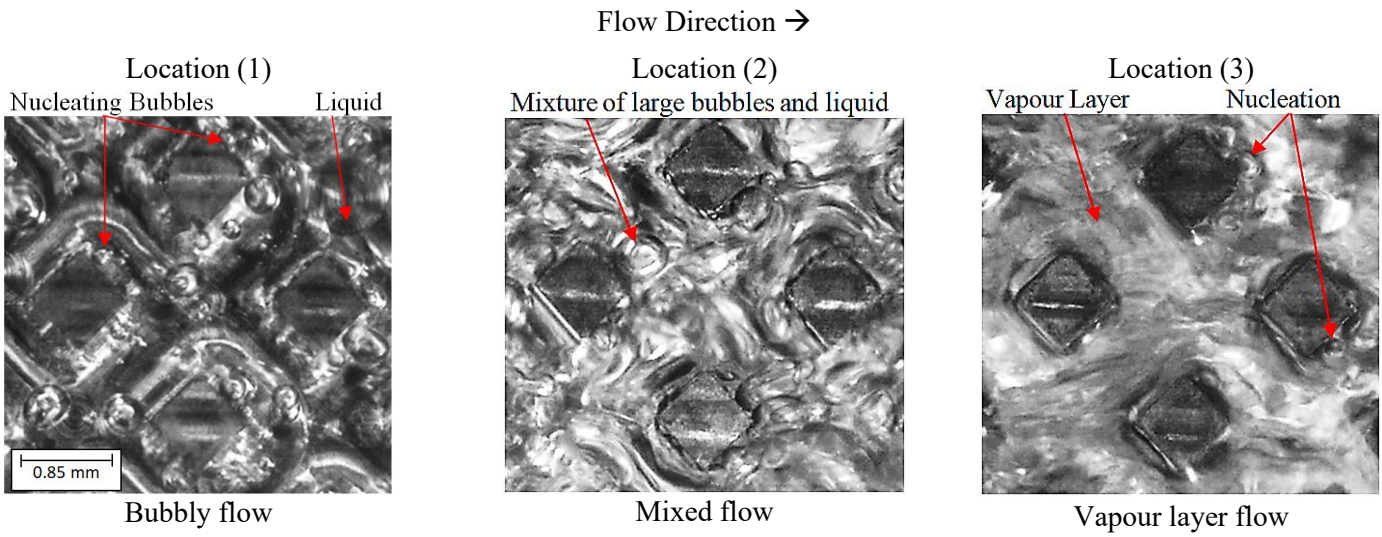



**Fig. 12** Flow patterns along the micro pins heat sink at inlet pressure of 1 bar, mass flux of 100 kg/m$^2$ s and wall heat flux around 47 kW/m$^2$, [40].

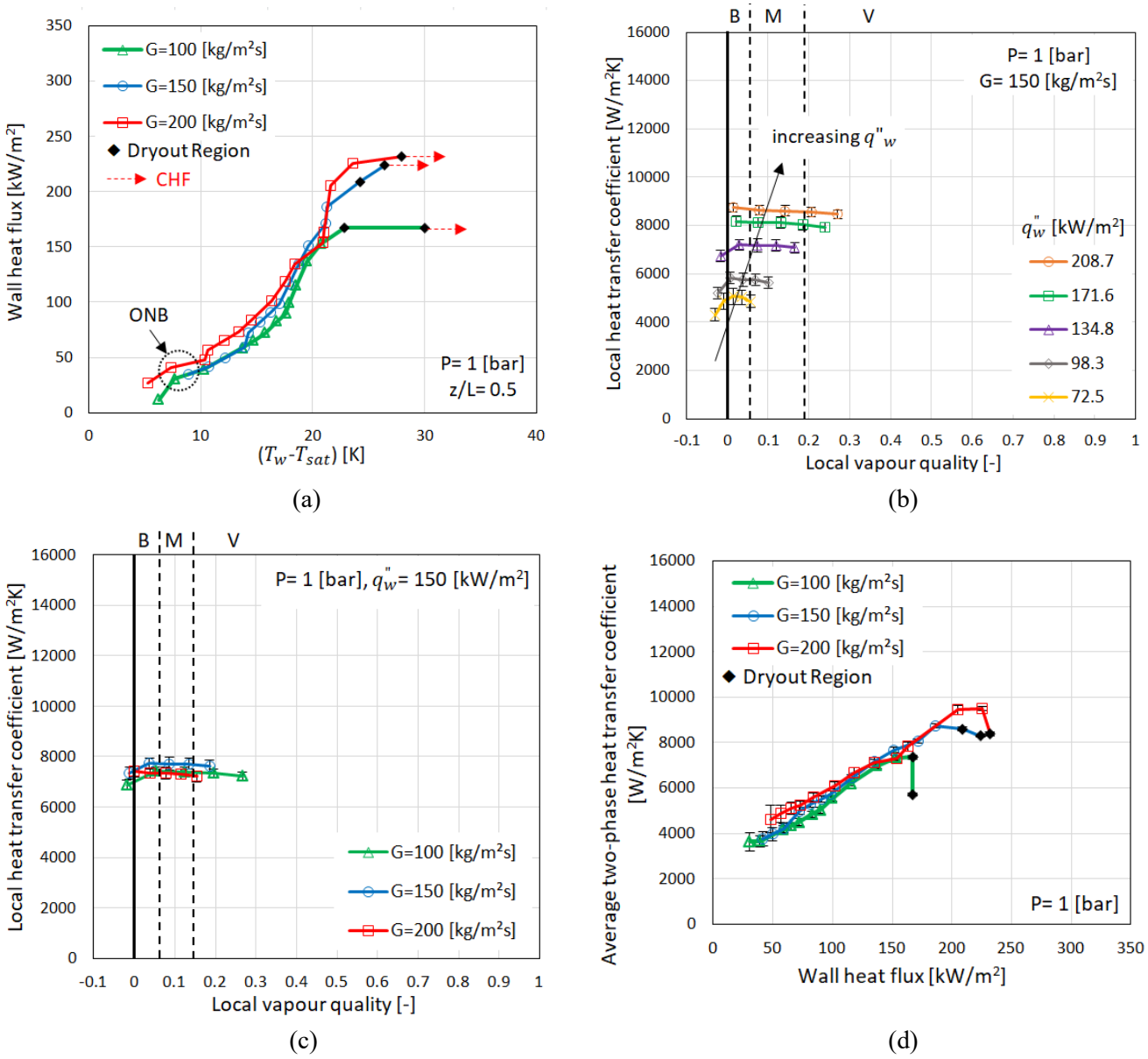



**Fig. 13** Experimental heat transfer results for the micro-gap heat sink:
(a) Boiling curve (b) Local heat transfer coefficient at different heat fluxes (c) Local heat transfer coefficient at different mass fluxes (d) Average two-phase heat transfer coefficient.
B: bubbly, M: mixed, V: vapour layer-liquid straps flow

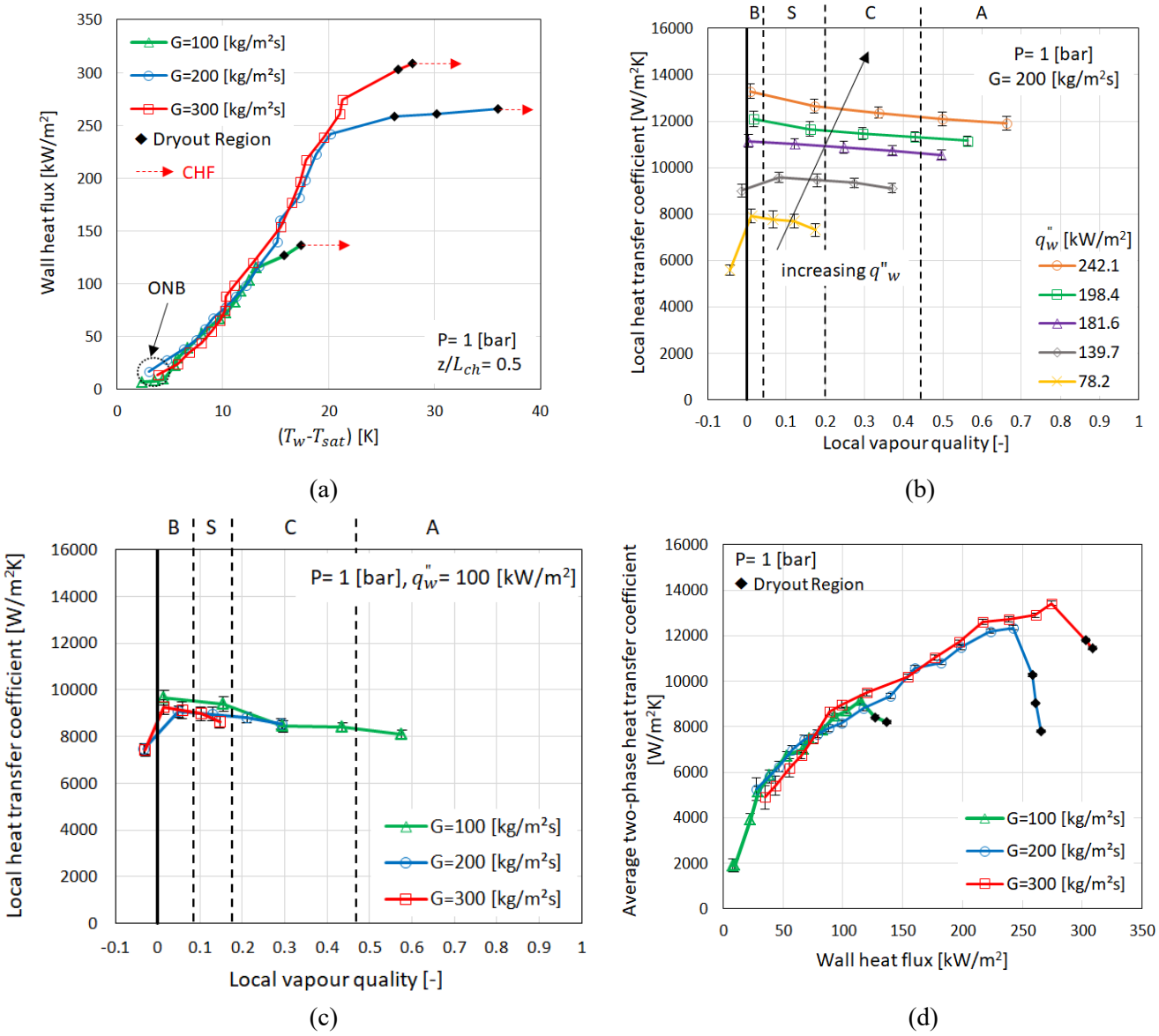



**Fig. 14** Experimental heat transfer results for the multi-channels heat sink:
(a) Boiling curve (b) Local heat transfer coefficient at different heat fluxes (c) Local heat transfer coefficient at different mass fluxes (d) Average two-phase heat transfer coefficient.
B: bubbly, S: slug, C: churn, A: annular flow

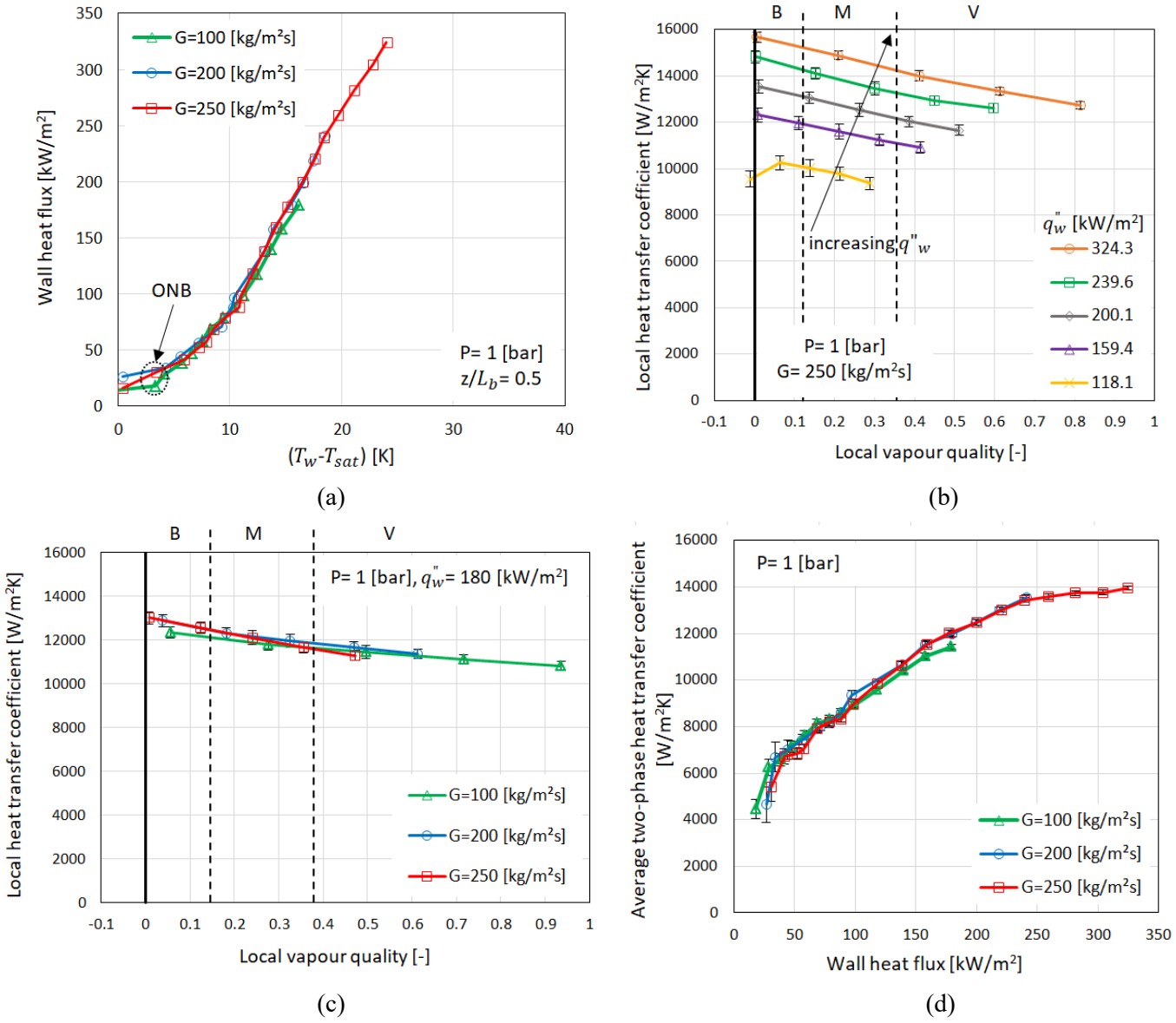



**Fig. 15** Experimental heat transfer results for the micro pins heat sink, [40]:
(a) Boiling curve (b) Local heat transfer coefficient at different heat fluxes (c) Local heat transfer coefficient at different mass fluxes (d) Average two-phase heat transfer coefficient.
B: bubbly, M: mixed, V: vapour layer flow

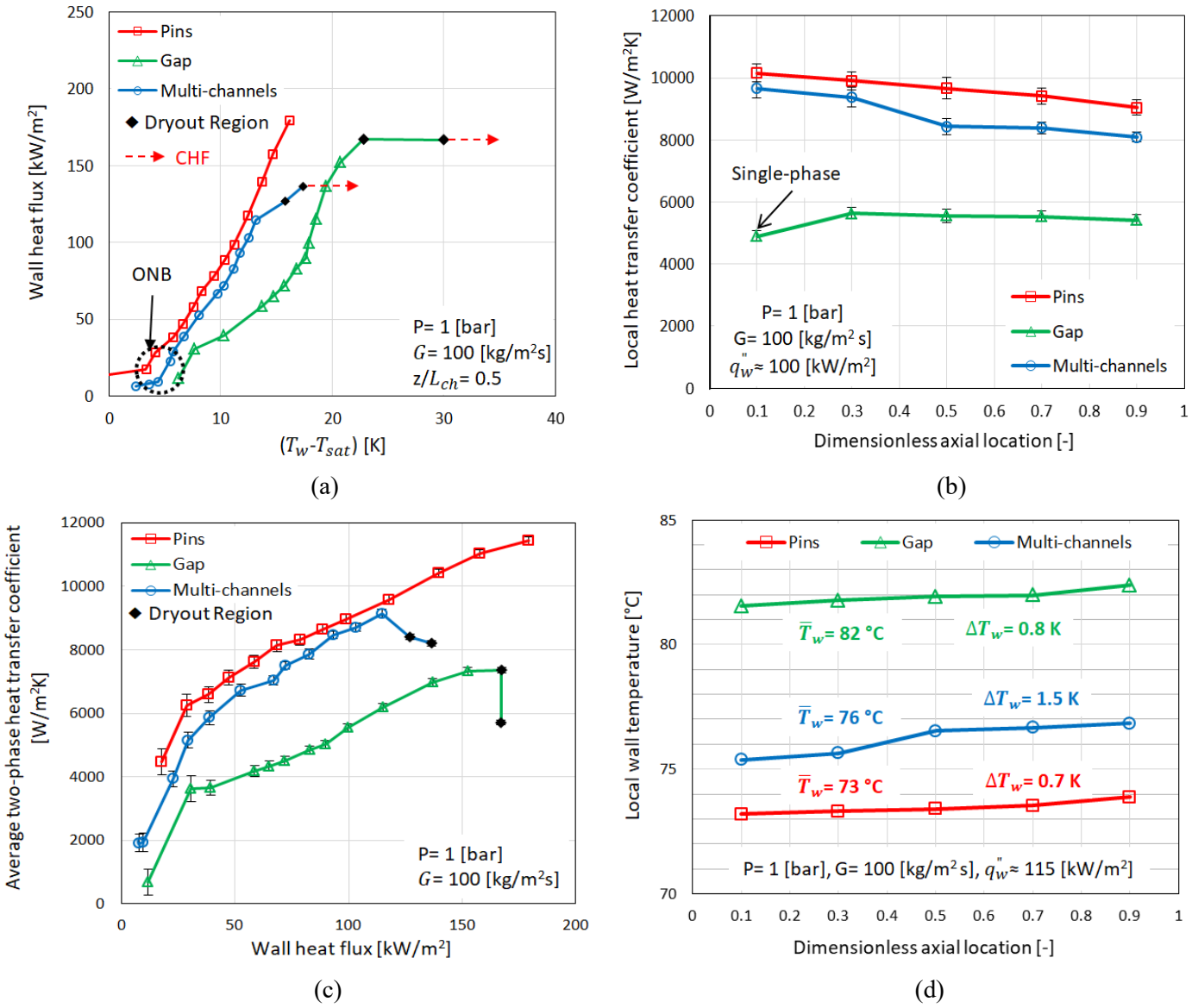



**Fig. 16** Comparison of heat transfer rates and temperature profile for the three heat sinks: (a) Boiling curve (b) Local heat transfer coefficient (c) Average two-phase heat transfer coefficient (d) Surface temperature distribution along the heat sink.

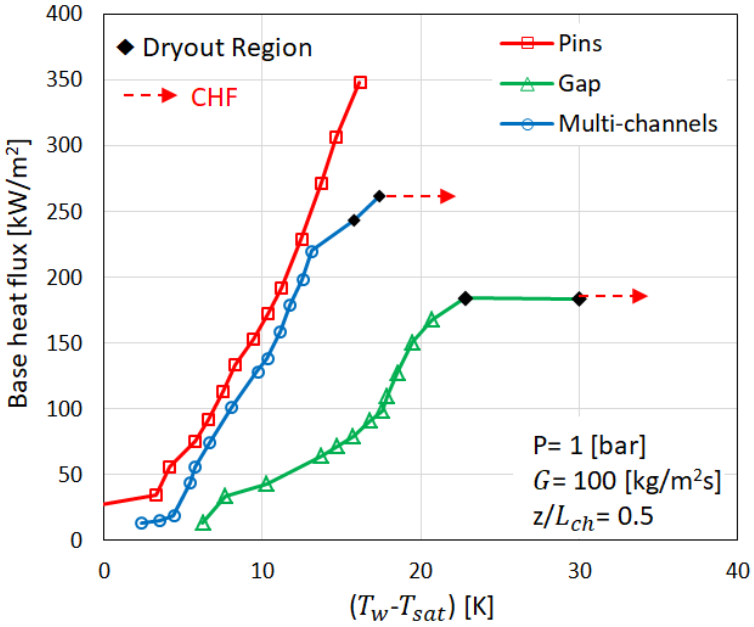
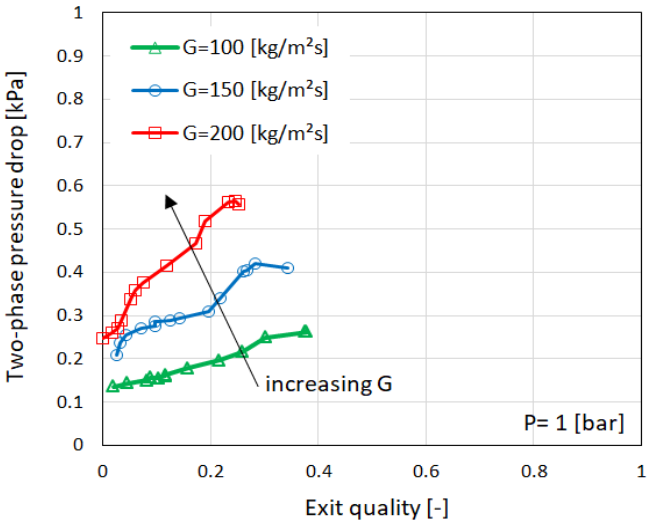
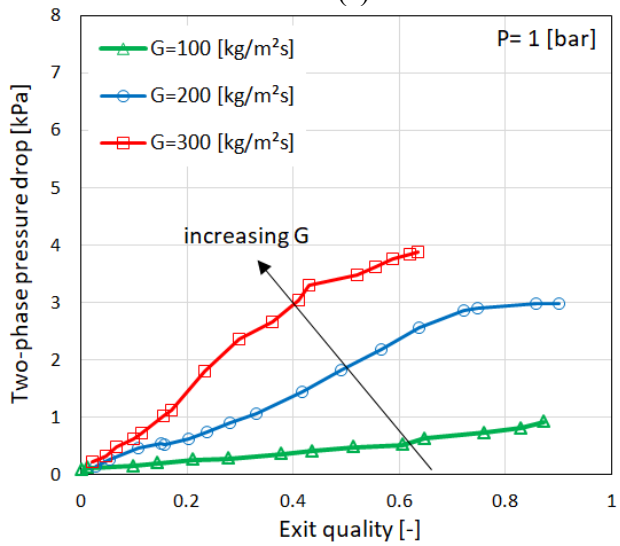


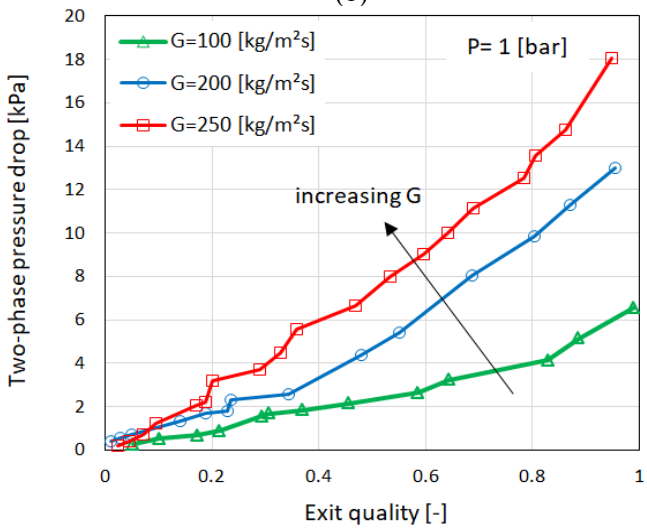

**Fig. 17** Base heat flux versus temperature difference for the three heat sinks.




(a)

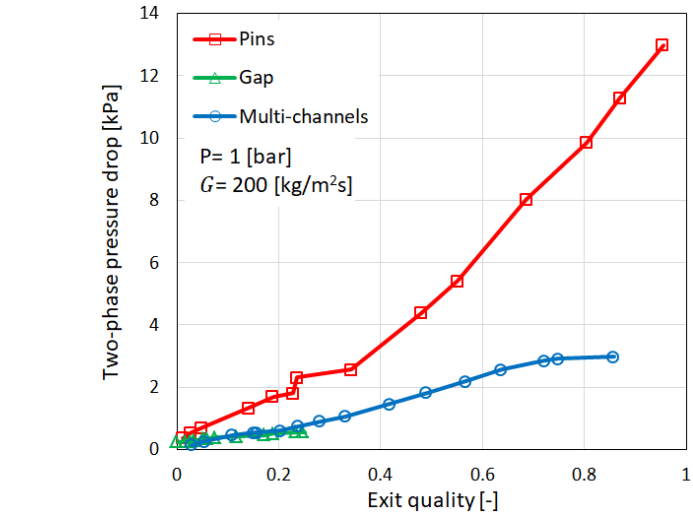



(b)

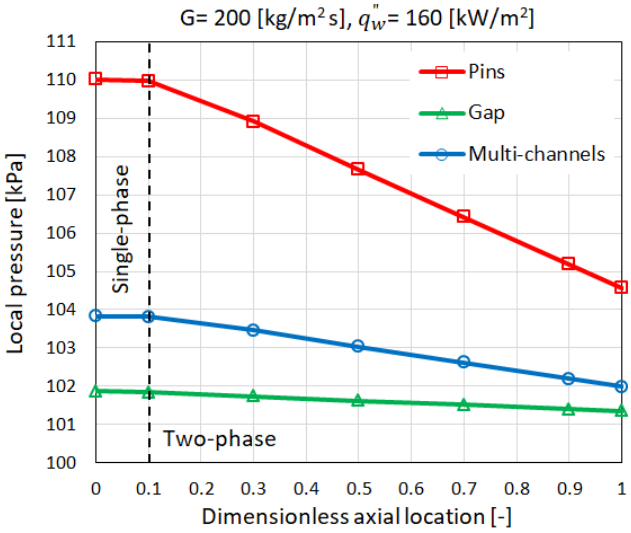



(c)

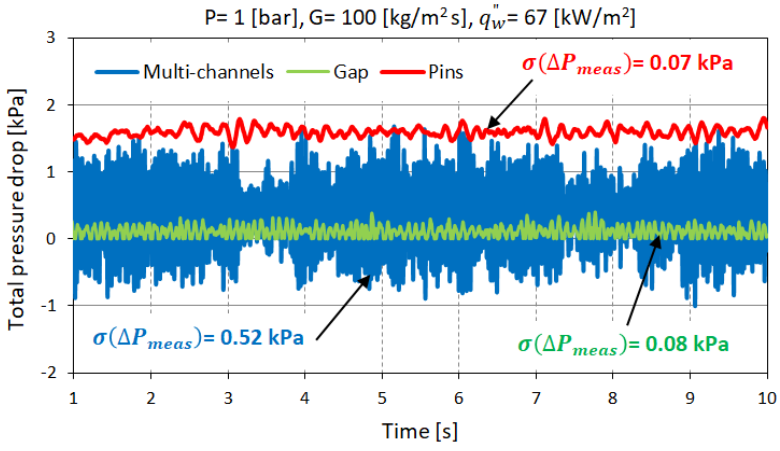
**Fig. 18** Experimental two-phase pressure drop:
(a) Micro-gap (b) Multi-channels (c) Micro pins fin, [40].




(a)

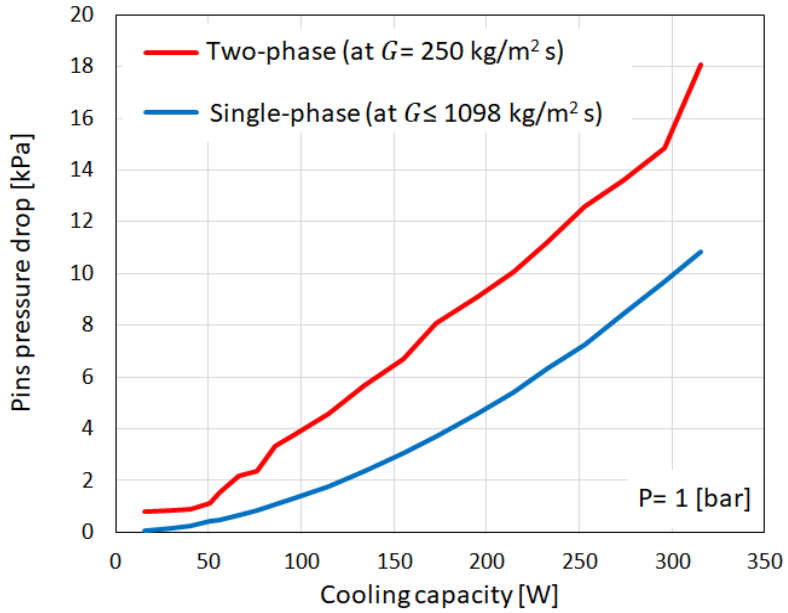



(b)

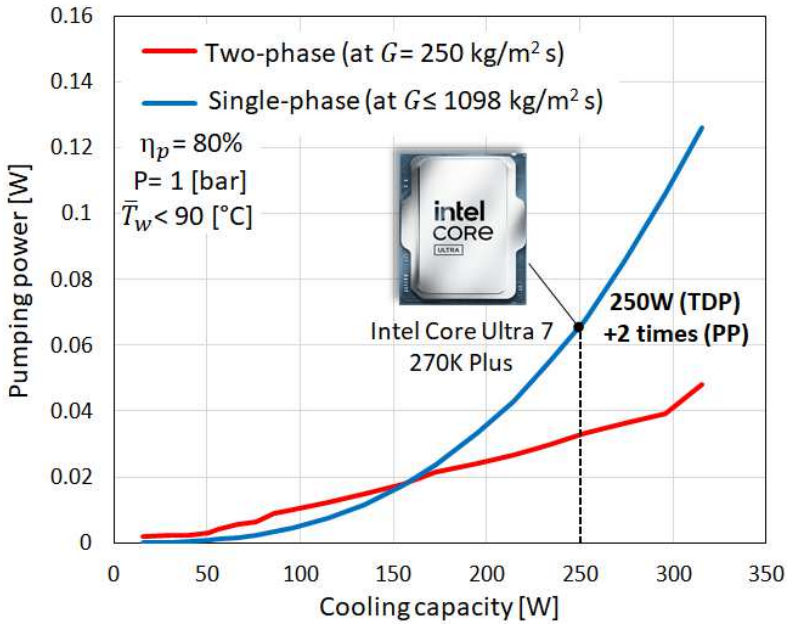



(c)

**Fig. 19** Comparison of pressure results for the three heat sinks:
(a) Two-phase pressure drop (b) Local total pressure (c) Signal fluctuation of the measured total pressure drop.




(a)




(b)

**Fig. 20** Comparison between single-phase and two-phase flow of the present micro pins heat sink: (a) Pressure drop (b) Pumping power (CPU image source: intel.com).